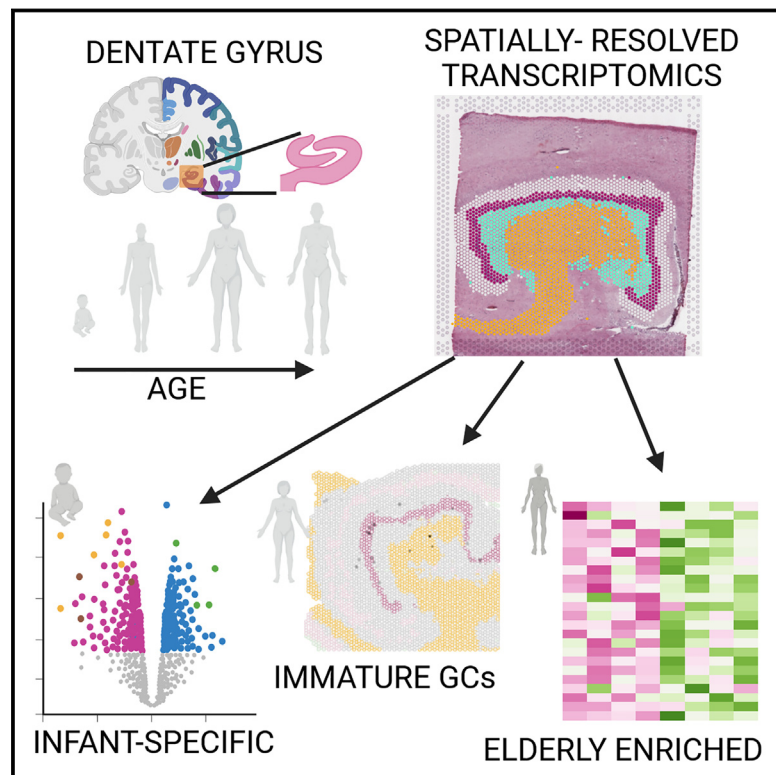


Spatiotemporal analysis of gene expression in the human dentate gyrus reveals age-associated changes in cellular maturation and neuroinflammation

Graphical abstract



Authors

Anthony D. Ramnauth, Madhavi Tippani, Heena R. Divecha, ..., Keri Martinowich, Stephanie C. Hicks, Stephanie C. Page

Correspondence

stephanie.page@libd.org

In brief

Ramnauth et al. generated transcriptome-wide spatial gene expression maps of the human dentate gyrus from infant, teen, adult, and elderly brain donors. They investigate subfield-specific gene expression patterns and identify age-associated changes in gene expression in the dentate gyrus.

Highlights

- Spatial transcriptomics from human dentate gyrus
- Donors across the lifespan
- Spatially resolved, age-associated gene expression changes



Resource

Spatiotemporal analysis of gene expression in the human dentate gyrus reveals age-associated changes in cellular maturation and neuroinflammation

Anthony D. Ramnauth,^{1,2} Madhavi Tippangi,¹ Heena R. Divecha,¹ Alexis R. Papariello,¹ Ryan A. Miller,¹ Erik D. Nelson,^{1,3} Jacqueline R. Thompson,⁴ Elizabeth A. Pattie,¹ Joel E. Kleinman,^{1,5} Kristen R. Maynard,^{1,2,5} Leonardo Collado-Torres,^{1,4} Thomas M. Hyde,^{1,5,6} Keri Martinowich,^{1,2,5,7,11} Stephanie C. Hicks,^{4,8,9,10,11} and Stephanie C. Page^{1,5,11,12,*}

¹Lieber Institute for Brain Development, Johns Hopkins Medical Campus, Baltimore, MD 21205, USA

²The Solomon H. Snyder Department of Neuroscience, Johns Hopkins School of Medicine, Baltimore, MD 21205, USA

³Cellular and Molecular Medicine Graduate Program, Johns Hopkins School of Medicine, Baltimore, MD 21205, USA

⁴Department of Biostatistics, Johns Hopkins Bloomberg School of Public Health, Baltimore, MD 21205, USA

⁵Department of Psychiatry and Behavioral Sciences, Johns Hopkins School of Medicine, Baltimore, MD 21205, USA

⁶Department of Neurology, Johns Hopkins School of Medicine, Baltimore, MD 21205, USA

⁷Johns Hopkins Kavli Neuroscience Discovery Institute, Baltimore, MD 21205, USA

⁸Department of Biomedical Engineering, Johns Hopkins School of Medicine, Baltimore, MD 21205, USA

⁹Center for Computational Biology, Johns Hopkins University, Baltimore, MD 21205, USA

¹⁰Malone Center for Engineering in Healthcare, Johns Hopkins University, Baltimore, MD 21205, USA

¹¹Senior author

¹²Lead contact

*Correspondence: stephanie.page@libd.org

<https://doi.org/10.1016/j.celrep.2025.115300>

SUMMARY

The dentate gyrus of the hippocampus is important for many cognitive functions, including learning, memory, and mood. Here, we present transcriptome-wide spatial gene expression maps of the human dentate gyrus and investigate age-associated changes across the lifespan. Genes associated with neurogenesis and the extracellular matrix are enriched in infants and decline throughout development and maturation. Following infancy, inhibitory neuron markers increase, and cellular proliferation markers decrease. We also identify spatio-molecular signatures that support existing evidence for protracted maturation of granule cells during adulthood and age-associated increases in neuroinflammation-related gene expression. Our findings support the notion that the hippocampal neurogenic niche undergoes major changes following infancy and identify molecular regulators of brain aging in glial- and neuropil-enriched tissue.

INTRODUCTION

Cognitive processes that depend on the dentate gyrus (DG) of the hippocampus (HPC) mature and decline over development and aging.^{1–7} The ability to form long-term memories is established in early childhood,^{8,9} while cognitive decline begins in late adulthood^{10–12} and accelerates in age-associated dementias.^{13,14} Development and deterioration of these cognitive functions are partially regulated by molecular, cellular, and anatomical processes in the DG that change across neurodevelopment.^{15,16} Specialized DG cell types are organized into distinct sub-domains. Glutamatergic granule cells (GCs) are densely packed within the GC layer (GCL) with dendrites that comprise the molecular layer (ML). A thin subgranular zone (SGZ) separates the GCL from the cornu ammonis 4 (hilus/CA4), which then relays information from the CA3 to the CA1 to the subiculum. The GCs in the GCL receive major excitatory inputs from the entorhinal cortex and regulate information flow into the HPC.^{1,2,17} This spatial heterogeneity results in regions dense with cell bodies of varying

cell types or sparse in cell bodies but enriched with synapses, termed neuropils.

In most mammalian species, a spatially defined neurogenic niche is retained in the adult DG. Proliferating radial glial-like stem cells reside in the SGZ and then differentiate and migrate as neuroblasts into the GCL during their development into mature GCs.¹⁸ While adult neurogenesis in the rodent is well established, the existence, abundance, and function of adult neurogenesis in the human DG remains controversial.^{19,20} Cell types representing the full developmental trajectory of neurogenesis (radial glial-like stem cells, migrating neuroblasts, and immature GCs [imGCs]) have been profiled using single-cell RNA sequencing (scRNA-seq) in mouse HPC.²¹ Similarly, single-nucleus RNA-seq (snRNA-seq) in macaque HPC identified all major neural precursor populations, but comparisons to mice suggested differences in neurogenic processes.²² While some immunohistochemical studies support the existence of adult neurogenesis in human HPC,^{23–31} others suggest an absence or paucity of newborn neurons.^{29,32–34} Recent studies using



transcriptomic strategies have not resolved this debate, with some studies providing evidence for newborn neurons,^{35–37} while others have not detected newborn neurons.^{38–41} Since snRNA-seq studies lack spatial context and omit extranuclear transcripts, findings regarding human DG adult neurogenesis remain inconclusive.

The DG undergoes dynamic changes with aging and is vulnerable to “inflammaging”—an age-associated increase in pro-inflammatory markers.⁴² Inflammation is associated with blood-brain barrier (BBB) permeability, and human studies suggest pronounced aging-related increases in BBB permeability at the DG.⁴³ In aged rodents, neuroblasts adopt a senescence-associated secretory phenotype that induces auto-inflammation,⁴⁴ while glial cells undergo age-associated neuroinflammation in the DG, which decreases neurogenesis and exacerbates degeneration.^{42,45–53} Importantly, activated microglia can induce reactive astrocytes,⁴⁸ triggering inflammation and neurodegeneration. However, molecular profiles of microglia in mouse models cannot fully recapitulate the transcriptomic phenotype of aged human microglia,⁵⁴ highlighting the importance of studies in human tissue.

To better address age-associated changes to the neurogenic niche and regional vulnerability to inflammaging, we used spatially resolved transcriptomics (SRT) to profile sub-domains of the human DG across four life stages (infant, teen, middle age, and elderly). SRT profiles intact tissue sections, capturing extranuclear transcripts and providing gene expression information within the coordinates of the existing architecture. We performed differential expression (DE) analyses across age groups at the level of the composite DG and individual sub-domains. The data reveal decreased neural proliferation, protracted development of inhibitory neurons and oligodendrocytes after infancy, and accelerated age-associated changes linked with neuroinflammation in glia-rich areas. To further explore spatio-molecular heterogeneity in the DG across the human lifespan, we provide full access to the data, code, and an interactive web application (https://libd.shinyapps.io/Lifespan_DG/).

RESULTS

Experimental design to investigate spatial gene expression in the human DG across the lifespan

To investigate spatio-molecular signatures across the lifespan, we binned donors into four age groups representing key developmental time points: infant (0–2 years), teen (13–18 years), adult (30–50 years), and elderly (70+ years). We dissected tissue blocks from fresh-frozen anterior HPC from 17 neurotypical donors (Table S1), scored each block to isolate the DG, and collected SRT data ($n = 17$ total capture areas; Figure 1A). We used standard quality control methods (Figures S1 and S2), excluding one sample (elderly donor Br3874) because the GCL was not present (Figures S2 and S3). Data preprocessing included normalization, feature selection, and batch integration (STAR Methods; Figure S4). The final dataset contained 68,685 spots from $n = 16$ donors.

To identify spatial domains, we performed unsupervised spatial clustering using BayesSpace at $k = 10^{55,56}$ and examined

the expression of canonical DG gene markers (Figures 1B, 1C, S5, and S6). We compared these predicted spatial clusters with manually derived annotations (Figure S7; Table S2) and found more precise delineation of spatial domains with unsupervised clustering (STAR Methods; Figure S8).

To identify differentially expressed genes (DEGs) across spatial domains, we pseudo-bulked spots (STAR Methods; Figure 1D) and performed principal-component analysis (PCA). A large fraction of variance was explained by spatial cluster 3, which mapped to the choroid plexus (CP) (STAR Methods; Figures 1C, S6, and S9A). PCA without CP illustrated that spatial domain followed by age group were the top components of variation (Figures 1E and S9B). Infant samples separated from all other age groups, highlighting a major developmental distinction associated with early life.

Identification of age-associated molecular signatures in the human DG

We generated a composite DG from the DG spatial domains (ML, GCL, SGZ, and CA3&4; STAR Methods; Figures 2A, S5, and S10) and performed DE analysis to compare each age group to all other age groups (Table S3). We identified that most DEGs were in the infant group ($n = 3,284$), followed by the elderly group ($n = 1,745$), and fewer DEGs with smaller fold changes were identified in the teen ($n = 462$) and adult ($n = 834$) groups (Figures 2B–2E). Interestingly, some genes associated with neurogenesis were significantly upregulated only in infancy, while genes associated with activated microglia and reactive astrocytes were downregulated in the infant and teen groups (Figures 2B and 2C) but upregulated in the adult and elderly groups (Figures 2D and 2E). This pattern suggests an inverse relationship between proliferative potential and glial inflammatory activity that changes with the onset of adulthood. We also noted the depletion of some inhibitory neuronal marker genes in the infant group that were enriched in the adult group, specifically *LAMP5* and *CCK* (Figures 2B and 2D).

Gene Ontology (GO) analysis further supported the increased proliferation of both neurons and glia in the infant group and enhanced neuroinflammation in adults, which persisted in the elderly group (Figure 2F; Table S4). With respect to proliferation, we note the upregulation of gliogenesis in the elderly group. GO terms for respiration-related processes were increased in the adult, but not the elderly, group, suggesting increased oxidative stress. The GO term for BBB maintenance was increased in the infant group, while response to ischemia was decreased in the infant and increased in the elderly groups, suggesting deterioration of vasculature and the BBB over age (Figure 2F). We also found reversals in GO terms from infancy to advanced age related to the development of synapses and dendrites, lysosomal membrane, synapse pruning, and the major histocompatibility (MHC) class II immune response (Figure 2F). Additionally, extracellular matrix (ECM) organization was only enriched in the infant group (Figure 2F). To determine the spatial heterogeneity of the observed changes in early postnatal development, we focused on infant samples to investigate changes across individual DG sub-domains.

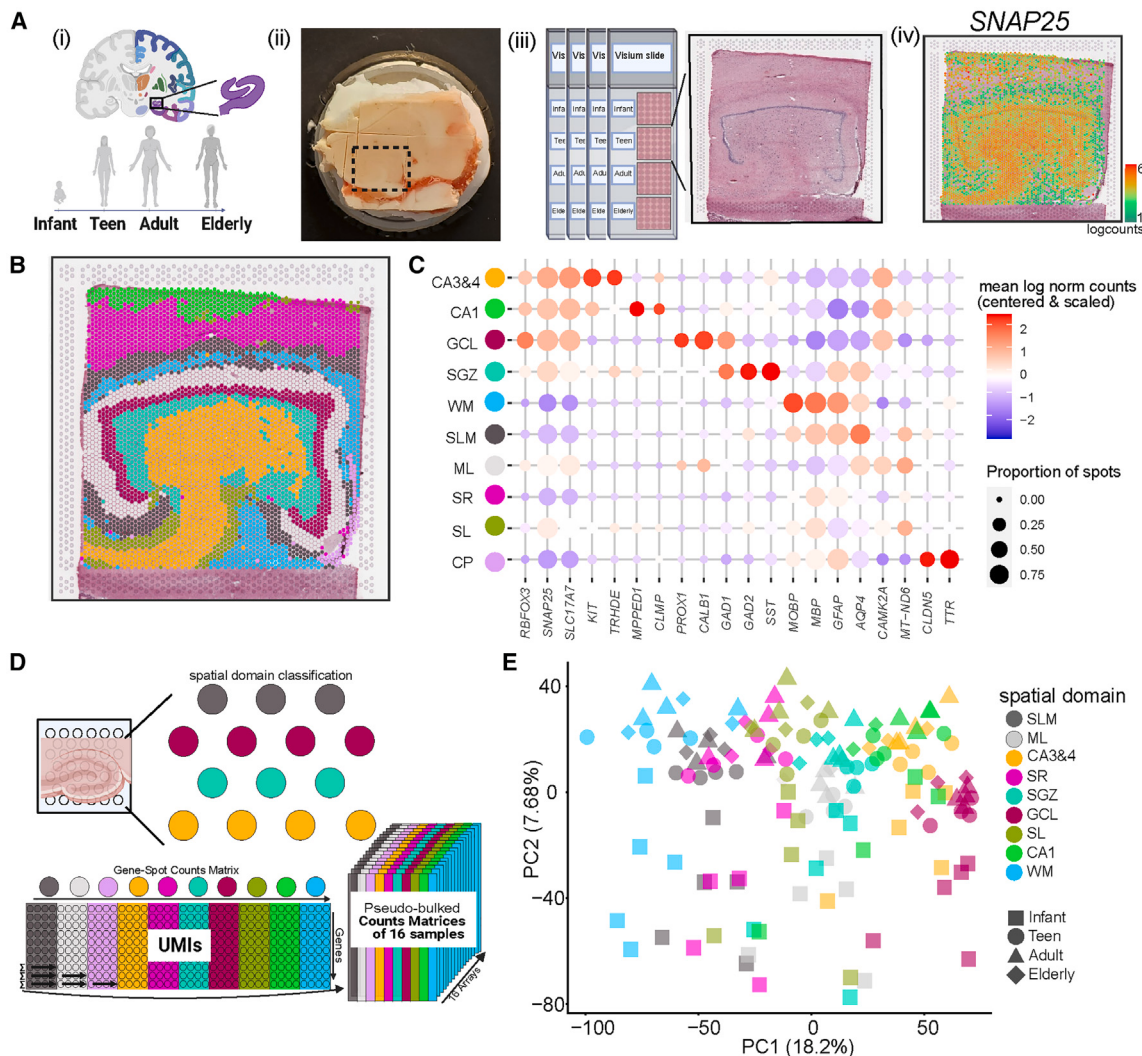


Figure 1. Spatially resolved transcriptomic profiling and unsupervised spatial domain detection in the human dentate gyrus across the postnatal lifespan

(A) Experimental design for acquiring SRT data in the human dentate gyrus (DG) across four age groups (i): infant (0–2 years), teen (13–18 years), adult (30–50 years), and elderly (70+ years). (ii) Dissected tissue blocks were scored to isolate the DG and then (iii) mounted onto Visium slides (10× Genomics) and stained. (iv) On-slide cDNA synthesis, followed by library construction and sequencing, provided spatially resolved gene expression, illustrated by SNAP25.

(B) Spots labeled by spatial cluster from Br1412.

(C) Gene expression across clusters. Dots are sized by the proportion of spots with non-zero expression and colored by mean log₂ normalized counts, centered, and scaled. CA3&4, cornu ammonis 3 and 4; CA1, cornu ammonis 1; GCL, granule cell layer; SGZ, subgranular zone; WM, white matter; SLM, stratum lacunosum-moleculare; ML, molecular layer; SR, stratum radiatum; SL, stratum lucidum; CP, choroid plexus.

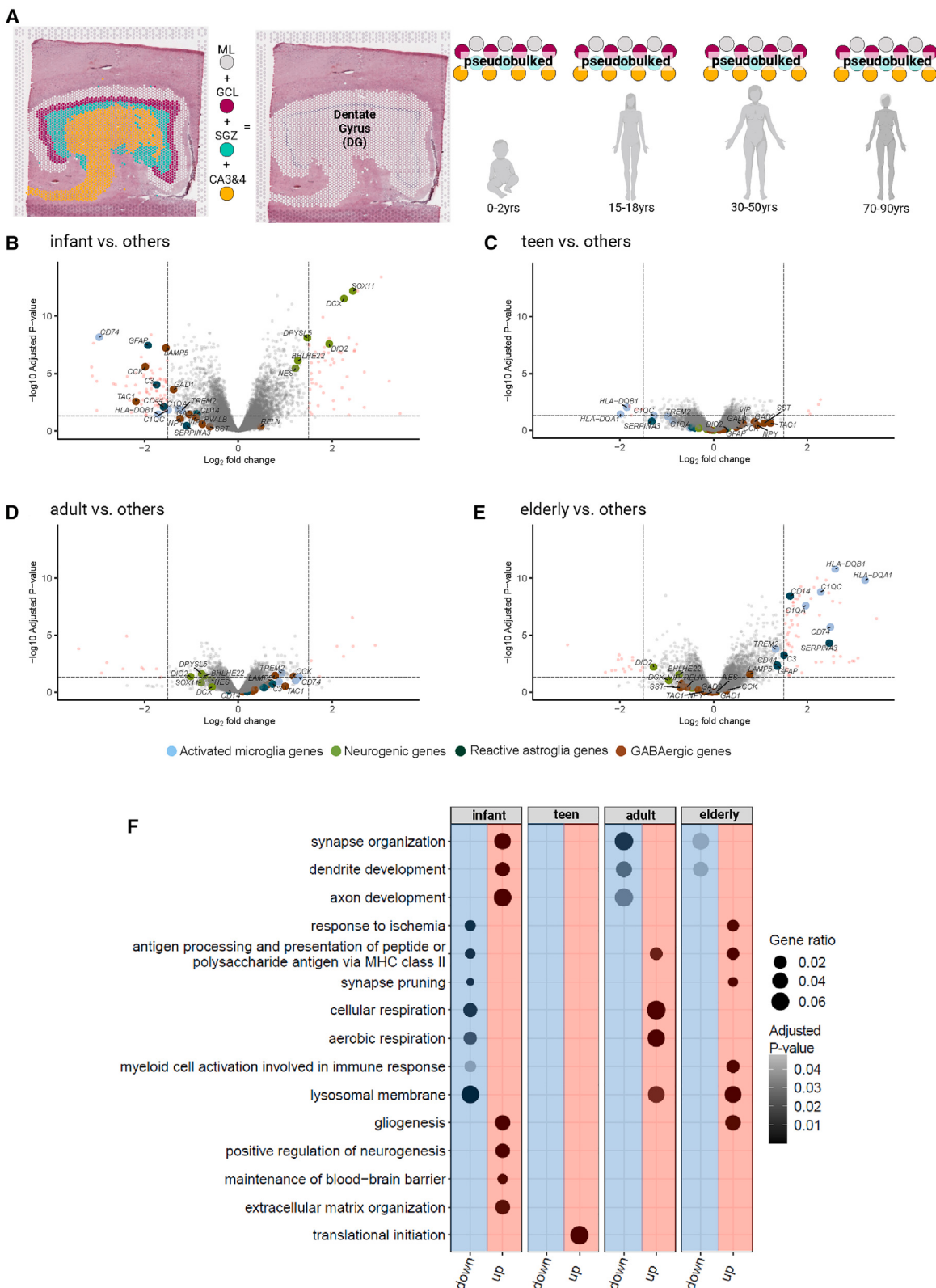
(D) Strategy for pseudo-bulking spots across all spatial domains from all donors.

(E) Scatterplot of the first two principal components (PCs) after pseudo-bulking, labeled by domain (color) and age (shape).

Age-associated changes in genes related to inhibitory neurons, neuronal proliferation, and ECM map to defined areas in the DG

While the analysis of pseudo-bulked DG sub-domains across age groups identified many of the same genes as the analysis of the composite DG, the spatial resolution was improved by mapping DE signals to specific DG sub-domains. Several genes associated with inhibitory interneuron markers were depleted in the infant group across DG sub-domains. While CCK was depleted in all DG sub-domains, GAD1 was depleted specifically

in the ML and GCL and *LAMP5* in the ML, GCL, and SGZ (Figures 3A–3D; Table S5). To support these findings, we queried existing bulk RNA-seq data from human HPC⁵⁷ and RNA-seq data from human GCLs isolated with laser-capture microdissection (LCM).^{41,57} CCK expression increased after infancy in our data as well as the bulk HPC RNA-seq dataset⁵⁷ (Figure S11). Following infancy, *LAMP5*, which marks a subpopulation of GABAergic inhibitory neurons,⁵⁸ showed unexpected expression in the GCL, which is primarily composed of excitatory neurons (Figure S11A). We observed increased *LAMP5* expression



(legend on next page)

over the lifespan in the bulk RNA-seq data⁵⁷ (Figure S11B) and found *LAMP5* enrichment in the GCL relative to the aggregate HPC in the LCM data⁴¹ (Figure S11C). We qualitatively validated these changes in *GAD1* and *LAMP5* expression in the GCL using single-molecule fluorescence *in situ* hybridization (smFISH) in infant and adult donors (Figures 3E and S12). We observed abundant *LAMP5* expression in *SLC17A7*-expressing excitatory neurons in the GCL as well as in *GAD1*-expressing inhibitory neurons in the SGZ, further supporting *LAMP5* expression in excitatory neurons.

Similar to the composite DG analysis, a comparison of the infant group vs. all other age groups yielded the most DEGs across individual DG sub-domains (Figures S13A and S14; Table S5). We ruled out that this finding was due to technical variables (Figures S13B–S13D), although the estimated cell counts per spot at the GCL are higher in the infant group, which may contribute to this finding (Figure S15). In contrast, the teen and adult age groups had few DEGs in each sub-domain (Figures S13A and S16; Table S5). However, because separating the DG into sub-domains decreases the number of spots per age group, this analysis may be underpowered to detect age-associated differences.

Although the infant group yielded the most DEGs (Figures S13A, S14, and S16; Table S5), we noted that the infant GCL had higher estimated cell counts (Figure S15) but ruled out that the increased DEGs were due to common technical confounders (Figures S13B–S13D). Given the paucity of DEGs from the other age groups, we asked if we could find gene expression gradients across age for each DG spatial domain by combining the top DEGs unique to infants (infant vs. all others) for all DG sub-domains (Figure 3F). This illustrated rapid decreases after infancy in the expression of many canonical neurodevelopmental markers, including *SOX4*, *SOX11*, and *IGFBP2*. Expression of doublecortin (*DCX*), a marker of imGCs frequently used as a proxy of neurogenesis, markedly decreased after infancy (Figure S17A), in line with previous findings.^{38–40} We likewise noted that *DCX* expression rapidly decreased with age in the bulk HPC RNA-seq dataset⁵⁷ (Figure S17D). One of the most significantly depleted genes in infancy was *METTL7B*, which increased with age in excitatory neurons in a human HPC snRNA-seq dataset.³⁹ In our data, *METTL7B* expression was depleted in the infant ML and SGZ and increased with age (Figure 3F). We found enrichment of many ECM-related genes in infant ML, SGZ, and GCL, including *POSTN*, *PTN*, *WIF1*, *COL1A2*, *BCAN*, *COL6A1*, *HAPLN1*, *SERPINH1*, and *NPNT* (Figures 3A–3D; Table S5). Expression of *POSTN*, which encodes the neurogenesis-associated cell adhesion molecule periostin,⁵⁹ declined with age in the bulk RNA-seq data⁵⁷ and was enriched in the GCL in the LCM data⁴¹ (Figures 3A, 3B, and S17).

To further investigate neurogenesis across the human lifespan, we collated molecular profiles generated from mouse, ma-

caques, and humans^{21,22,36} representing discrete GC maturation stages—neural progenitor cells (NPC), neuroblasts (NB1 and NB2), imGCs, mature GCs (GCs)—and conducted gene set enrichment analysis in human DG sub-domains across age groups. A gene set for mouse NB2 was the earliest stage in the maturation trajectory that showed consistent enrichment in the human GCL in all age groups (Figure S18A). However, many of the genes included in this set were not restricted to the SGZ but also expressed in other DG sub-domains (Figure S18B). A human snRNA-seq imGC gene set⁶⁰ showed the strongest enrichment in CA3&4, which decreased to non-significant enrichment in the elderly group (Figure S18A). In contrast, a separate gene set for imGCs derived from macaque²² showed consistent enrichment in the GCL for all age groups (Figures S18A and S18C). Together, these data show that although genes associated with neurogenesis in other species are expressed in the human HPC throughout the lifespan, they are not spatially restricted to the neurogenic niche.

NMF-based transfer learning from publicly available datasets suggests continued presence of imGCs in adulthood

To extend our gene set enrichment analyses, we asked if neurogenesis signatures could be explored with other computational strategies. Non-negative matrix factorization (NMF) is a dimensionality reduction technique that can identify coordinated patterns of gene expression, which can then be detected in another dataset via transfer learning.⁶¹ We recently identified 100 NMF patterns in adult human HPC snRNA-seq data and then integrated these patterns with paired SRT data from adjacent HPC tissue sections.⁶² Here, we investigated three patterns (nmf26, nmf5, and nmf14) that were enriched in sequentially overlapping subsets of GCs (nmf26 partially overlaps nmf5, which partially overlaps nmf14) (Figure 4A). Projection of these three patterns into the paired adult Visium data⁶² showed that, while all three patterns were restricted to the GCL (Figure 4B), nmf26 weights were more sparsely distributed. We compared unique gene markers for these three specific patterns to better understand biological relevance (Figure S19). Interestingly, many genes that are uniquely top weighted in nmf26 are also DEGs that are significantly increased in the infant DG (Figures 4C and 2; Table S3), including *POSTN* (Figure S17), *RASGRF2*, *DSCAML1*, *WIFP3*, *NREP*, and *GRID1*. Other highly weighted gene markers for nmf26 included *ALDH1A2*, *NRG3*, and *NEGR1* (Figure 4C). Meanwhile, many genes uniquely top weighted in nmf14 were significantly increased DEGs in the elderly DG (Figure S19).

Projecting the three patterns into the lifespan SRT data revealed that all three were spatially restricted to the GCL, but each pattern was strongly age associated (Figures 4D, 4E, and S19). Nmf26 was expressed in many spots throughout the infant

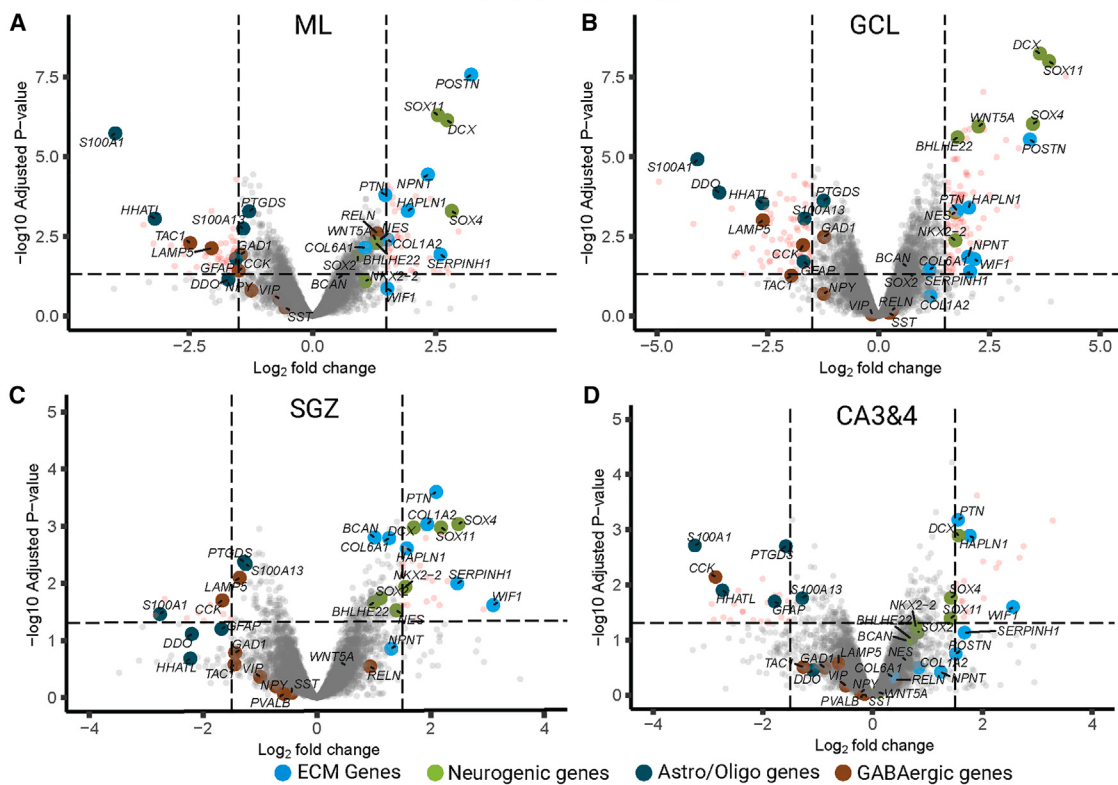
Figure 2. Differential expression analysis of composite DG identifies genes associated with age group (infant, teen, adult, and elderly)

(A) Pseudo-bulked spatial domains for ML, GCL, SGZ, and CA3&4 were collapsed to generate a composite DG profile for each donor.

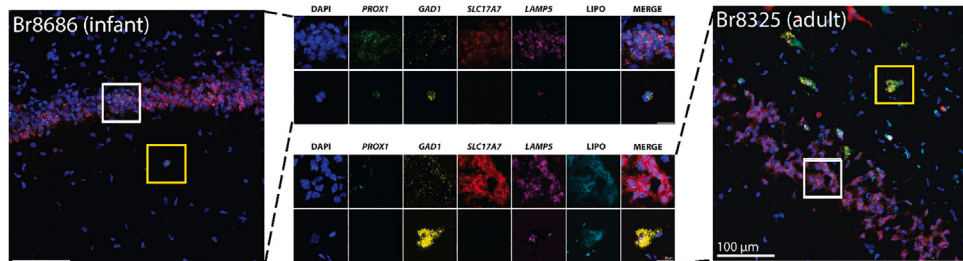
(B–E) Composite DG volcano plots illustrate DEGs from comparisons of each age group to all others. Colored points highlight genes associated with neurogenesis (green), activated microglia (light blue), reactive astroglia (dark green), and inhibitory neurotransmission (brown). The x axis is \log_2 fold change (FC) in expression, and the y axis is negative \log_{10} adjusted p values; red points indicate genes ≥ 1.5 or ≤ -1.5 logFC.

(F) Dot plots for Gene Ontology (GO) terms, faceted by age groups. Down- and upregulation columns are colored blue and red, respectively; dot size represents the gene ratio (fraction of gene set that was differentially expressed), and black gradient represents adjusted p value.

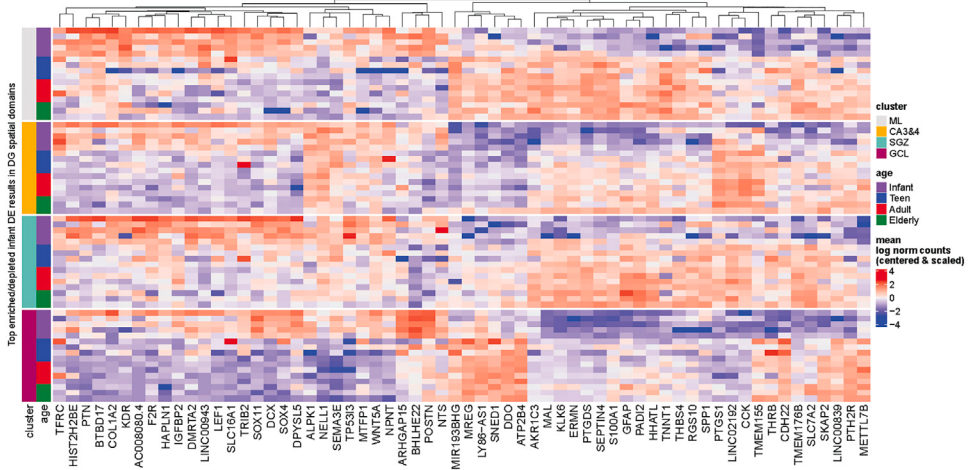
infant vs. others



E



F



(legend on next page)

GCL with high weights but present in fewer spots and at decreased weights in the teen, adult, and elderly groups. Nmf5 and nmf14 showed increased prevalence and higher weights at the GCL with age, although nmf5 peaked in adulthood, while nmf14 was primarily restricted to the elderly group. Projecting these patterns onto adult macaque DG scRNA-seq data²² revealed that nmf26 weights were enriched in a subset of NB and imGCs, while nmf5 and nmf14 weights were enriched in mature GCs (Figures S20A and S20C). Likewise, nmf26 weights were enriched in juvenile and imGCs from mouse neurogenic data,²¹ while nmf14 was largely absent (Figures S20B and S20D). Together, these data support the existence of a GC maturation trajectory. Specifically, nmf26 captures imGCs that are abundant in the infant, nmf5 represents the majority of mature GCs, and nmf14 captures aging GCs that are enriched in the elderly.

As depicted in the uniform manifold approximation and projection (UMAP) of the adult HPC human snRNA-seq data from which the NMF patterns were identified,⁶² nmf26 (infant associated) and nmf14 (non-infant associated) are enriched in different GC clusters (GC.3 and GC.4, respectively; Figure 4A).⁶² To identify genes that distinguish these two cell types, we explored pseudo-bulked DEG lists from GC.3 and GC.4, described previously,⁶² to identify genes unique to each cluster (Figure S21A). Interestingly, DEGs unique to GC.3 included neurogenesis-related genes, including *POSTN* and *FST*.⁶³ GO analysis of these DEGs highlighted opposing, functional differences between GC.3 and GC.4 related to development, cellular signaling, RNA translation, and ECM (Figure S21B). For example, neurogenesis and neuron differentiation GO terms were simultaneously down- and upregulated in GC.3, while the GO term for generation of neurons was downregulated, suggesting that GC.3 neurons are maturing as opposed to proliferating (Figure S21B). GC.3 also exhibited functional enrichment of GO terms related to synaptic plasticity and transmission, suggesting that GC.3 cells may be more primed for plasticity compared to GC.4 (Figure S21B). Many terms for development and differentiation were downregulated in GC.4, suggesting that neurons in the GC.4 cluster are more mature than GC.3 (Figure S21B).

Neuroinflammatory cell abundance and activity is a robust signature of aging in the DG

We noted a decrease in gene signatures associated with neurogenesis and a concurrent increase in gliogenesis-related gene expression over aging (Figures 2, 3, and 4). This included significant depletion of pan-glial gene expression in specific DG sub-fields in infancy, including *GFAP* in the ML, GCL, and CA3&4; *TMEM176* in the ML, SGZ, and GCL; *S100A1*, *S100A13*, and *PTGDS* in all DG sub-domains; and *HHATL* in the ML, GCL, and CA3&4 (Figures 3A–3D; Table S5). We also observed enrich-

ment of GO terms associated with MHC class II peptides in the composite DG of the elderly group (Figures 2E and 2F). Since MHC class II peptides are expressed in late-stage activated microglia,⁵⁰ we hypothesized that activated microglia may be more abundant in elderly donors. We collated gene markers for activated microglia^{50,64} and performed spatial enrichment analysis. Activated microglia associated genes were enriched in white matter (WM)- and neuropil-rich spatial domains, including the ML, stratum lucidum (SL), stratum lacunosum-moleculare (SLM), and stratum radiatum (SR) (Figure 5A). Many genes involved in the MHC class II immune response also showed age-associated increases in specific DG sub-domains (Figure 5B). Investigating elderly specific DEGs in each DG sub-domain show that many upregulated genes are related to microglia, natural killer (NK) cells, and reactive astrocytes (Figures 5C–5F), with enrichment in the ML (Figure 5C). Microglial marker genes were generally upregulated, including *C1QB* and *IL4R*⁵⁴ in the ML (Figure 5C) and in CA3&4 (Figure 5F) of the elderly group. Several genes were enriched in the composite DG of the elderly group but not significantly enriched in any individual sub-domain, including *CD74*, a reactive microglia marker⁵⁰ (Figure 2D) with increased expression in all DG sub-domains (Figures 5B and S22A). We confirmed this finding by querying bulk HPC RNA-seq data⁵⁷ for *CD74* expression with age (Figure S22B). The microglial marker *TREM2* and *HAMP*, which encodes hepcidin and is associated with iron sequestration in microglia and neurons, were enriched in the composite DG of the adult and elderly groups (Figures 2D and 2E; Table S3).

We observed a variety of immune-related gene expression in elderly samples, including genes expressed in activated human microglia and other immune-related cell types. For example, *FCGR3A*, which is enriched in elderly ML, SGZ, and CA3&4 (Figures 5C, 5E, and 5F), regulates the survival and proliferation of NK cells.^{65,66} To investigate changes in estimated cell proportions, we applied the spot-level deconvolution method cell2location⁶⁷ to publicly available human DG snRNA-seq data³⁹ (STAR Methods; Figures S23–S25). We found an increasing proportion of microglia and T cells in the SGZ with age (Figure S26).

Activated microglia can induce reactive astrocytes,⁴⁸ and reactive astrocyte gene markers are enriched in the composite elderly DG, including *GFAP*, *C3*, *SERPINA3*, *EMP1*, *CD109*, *CD44*, *SERPING1*, and *FKBP5* (Figure 2E; Table S3). Additional genes associated with reactive astrocytes show spatial specificity, including *S100A10* in the ML and *CD14* in the elderly ML, SGZ, and CA4&3 (Figures 5C–5F; Table S5). We also investigated changes in estimated cell proportions for glial populations across aging using spot-level deconvolution (STAR Methods). Cell2location estimated an age-associated increase in the proportion of oligodendrocytes in the ML, SGZ, and CA3&4 (Figure S27A) and in both *GFAP*⁺ and *GFAP*⁻ astrocytes in the

Figure 3. Differential gene expression of infant vs. all other age groups across DG sub-domains

(A–D) Volcano plots of infant vs. non-infant for ML (A), GCL (B), SGZ (C), and CA3&4 (D). The x axis is \log_2 fold change in expression, and the y axis is negative \log_{10} adjusted p values.
 (E) Representative smFISH images of GCL from infant (left) and adult (right) for *PROX1* (green), *GAD1* (yellow), *SLC17A7* (red), *LAMP5* (magenta), and lipofuscin autofluorescence (LIFO; cyan). Squares denote inset (top: white, bottom: yellow). Scale bars: 100 μm and 20 μm (inset).
 (F) Heatmap of mean \log_2 normalized counts (centered and scaled) for top 5 infant enriched and depleted genes with ≥ 1.5 or ≤ -1.5 logFC from each pseudo-bulked DG sub-domain. Hierarchical clustering was performed across columns. Rows are organized by spatial domains and age.

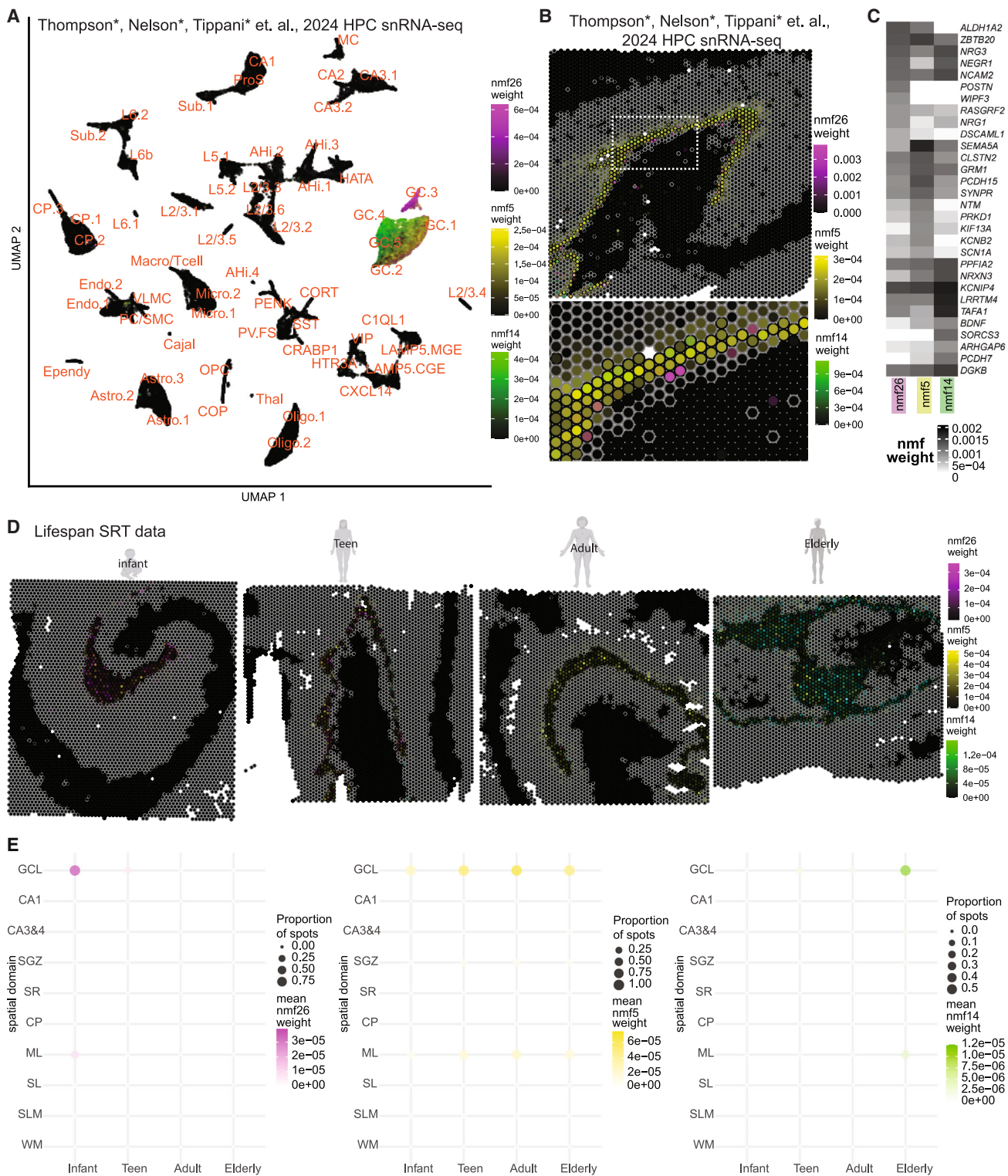


Figure 4. NMF patterns approximate a maturation trajectory for human dentate granule cells

(A) UMAP of human adult HPC snRNA-seq dataset⁶² with superfine cell class annotations. Nuclei are colored by weight of NMF patterns. Overlapping gradients of weights from multiple NMF patterns appear as blended.

(B) Representative spot plots from the adult HPC SRT dataset.⁶² GCL, CA3&4, and CA1 domains are outlined black; other domains are outlined gray. Spots are colored by weight of NMF patterns. Inset (bottom) is zoomed into the GCL.

(legend continued on next page)

ML and SGZ (Figures S27B and S27C). Taken together, these results suggest the enrichment of activated microglia and other neuroinflammatory markers in specific HPC spatial domains and spatially restricted vulnerability to age-associated gene expression changes within DG sub-domains (Figure 5A).

A minimal gene set tracks widespread hippocampal tissue changes with aging

Given the strong associations of many specific gene markers with age-associated processes, including proliferation and inflammation (Figures 2, 4, and 5), we asked if a minimal set of genes could track the spatial domains where gene expression is most dynamic over aging. Previous comparisons of bulk and snRNA-seq profiles from microdissected brain regions from mice across aging, paired with SRT profiles, identified WM-rich spatial domains as most vulnerable to age-associated gene expression changes.⁶⁸ We adapted their data-driven workflow⁶⁸ to compare older age groups to the infant age group within each human HPC spatial domain to compute a common aging score (CAS). Each CAS is a single value that represents the difference in transcriptional programs between biological conditions; in our case, infant vs. each other age group (STAR Methods). To obtain DEGs for computing the CAS, we leveraged all SRT spots and included all HPC spatial domains in our samples (STAR Methods; Table S6), identifying an age-associated gene set that included the neurogenesis-related markers DCX, SOX11, and SOX4, which decrease with age. Other DEGs increased with age, including oligodendrogenesis markers MAL and OPALIN and markers associated with MHC class II and inflammatory signaling (Figure 6A). GO analysis of these aging DEGs suggested the downregulation of neural proliferation paired with the upregulation of inflammatory activity and myelination (Figure 6B).

Using this widespread aging gene set as input, we computed the CAS for each gene expression spot in all donors in our study (Figures 6C, 6D, S28, and S29).⁶⁹ We then ordered CAS values for each spot by age for each spatial domain. The trajectory of these values rapidly increased from infancy to teen for all spatial domains, although the increase and variability were larger in glial- and neuropil-enriched spots (Figure 6C). We observe the largest changes in CASs in WM spots, which also have more CAS heterogeneity (Figures 6C and 6D). This implies localized changes over aging within WM. It is important to note that our human DG DEGs and CAS results did not take into account changes in cell density with age, which have decreasing trends for the GCL and increasing trends for WM (Figure S15). CAS values derived from the mouse study⁶⁹ show similar spatial heterogeneity (Figure S31A) but are not as sensitive to oligodendrocyte-rich spots (Figures 6C, 6D, S29, S30, and S31B), as they were limited to adult mice. To assess if the CAS was solely driven by cell type changes over the lifespan, we investigated the relationship between the CAS and cell type proportions in each spot and found that the predicted cell type proportions did not explain these findings (STAR Methods; Figure S30).

CAS trajectories can be approximated with linear modeling,⁶⁸ and the resulting slope can be used to infer a “CAS velocity” for each spatial domain (Figure 6E). We used the slopes to compare age-associated changes in CASs across spatial domains, where a higher slope indicates a higher rate of aging-associated changes in gene expression as captured by our DEGs (Figure 6F). The CAS baseline (i.e., CASs assigned to the infant spots) did not strongly predict a spatial domain’s CAS velocity across age, similar to previous data from mice.⁶⁸ Comparing CAS velocities for each spatial domain, we found that glial-enriched spatial domains had the largest CAS velocities, followed by neuropil-enriched spatial domains (Figure 6G), in agreement with the mouse study.⁶⁸ Of note, the ML, the most neuropil-enriched spatial domain in the DG, had a significantly larger CAS velocity than any other DG domain. This highlights the importance of retaining cytoplasmic transcripts, which are captured in SRT approaches but not snRNA-seq (Figure 6G). The differences in CAS velocities between spatial domains suggest that the human HPC exhibits differential aging within its sub-domains and that glial-enriched and neuropil-enriched domains exhibit a greater degree of aging-related changes in gene expression. This is consistent with our results suggesting increased microglia abundance and microglia-related gene expression signatures over aging.

DISCUSSION

Our results provide insight about age-associated changes in ECM composition, density, and localization across the DG spatial topography. In the infant, we observed an increased abundance of genes encoding ECM-related molecules implicated in HPC function during development. For example, PTN (pleiotrophin) and its receptor PTPRZ1 are associated with increased DG neurogenesis in a mouse model of senescence following environmental enrichment.^{70,71} *Halpn1* (hyaluronan and proteoglycan link protein 1) promotes the maturation of perineuronal nets surrounding parvalbumin+ interneurons in mouse dorsal CA1, resulting in enhanced neuronal allocation and memory precision.⁷² Periostin (POSTM) promotes neural stem cell proliferation as well as neuronal and astroglial differentiation *in vitro*, and intracerebroventricular injection after hypoxic-ischemic injury stimulates neural stem cell proliferation and differentiation in the SGZ.⁵⁹ Interestingly, *Postn* is not expressed after birth in the mouse DG,⁷³ suggesting a human-specific postnatal role. These infant-enriched ECM-related genes may represent potential targets for therapeutic strategies to stimulate cellular rejuvenation or proliferation.

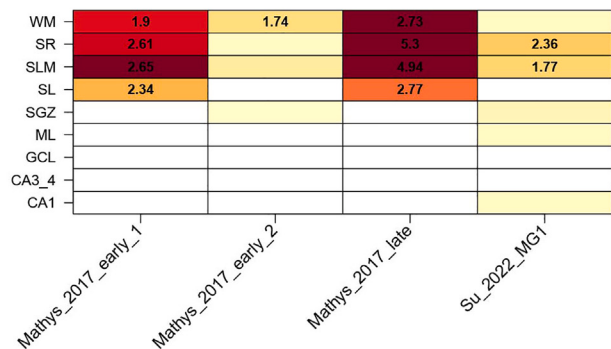
The existence of postnatal neurogenesis at the human GCL remains controversial.^{32,74} RNA-seq analysis of bulk homogenate^{57,75} or laser-captured⁴¹ postmortem human HPC tissue has not provided strong evidence for neurogenesis. However, low sensitivity limits the ability of these approaches to capture rare transcriptomic signatures. Some snRNA-seq studies in postmortem human HPC tissue²⁰ report a lack of evidence for

(C) Heatmap of gene-level NMF weights of top marker genes for nmf26, nmf5, and nmf14.⁶²

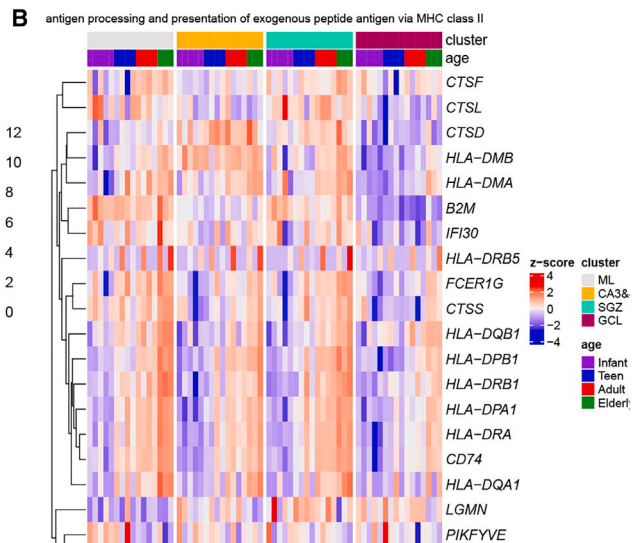
(D) Representative spot plots for each age group, colored by weight of nmf26, nmf5, and nmf14 and outlined as in (B).

(E) Dot plot of spatial domain vs. age group across all donors. Size represents the proportion of spots with non-zero pattern weights, and color represents mean pattern weight.

A

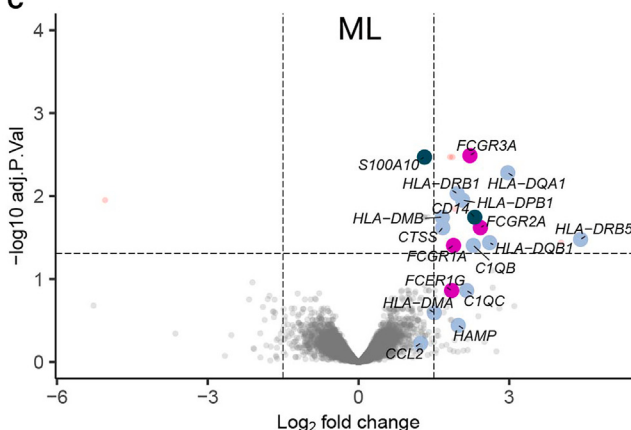


B

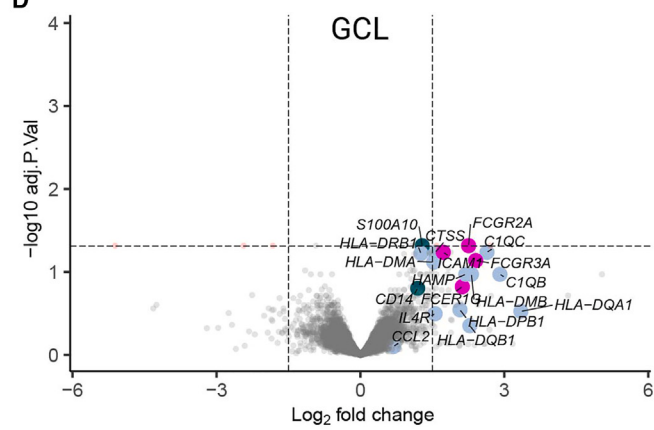


elderly vs. non-elderly

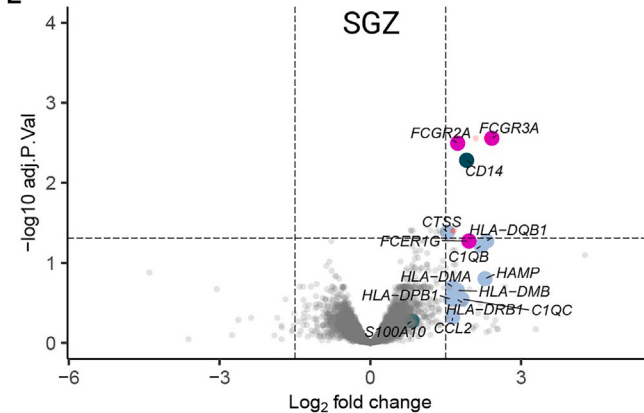
C



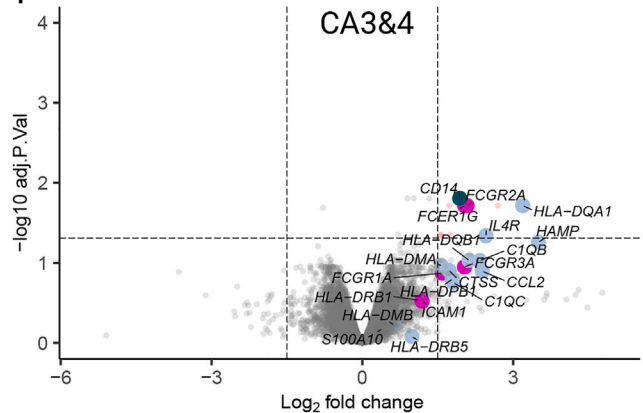
D



E



F



● Activated Microglia genes ● Natural Killer genes ● Reactive Astrocyte genes

(legend on next page)

neurogenesis,^{39,40,76} while others identify some cell types along the neurogenic trajectory.^{35,36,64,77} However, reanalysis of the data across these studies was inconsistent and identified differing cell populations.^{35,77} Moreover, a limitation of snRNA-seq is the inherent lack of spatial information and the inability to capture cytosolic transcripts. While the relatively small sample size of our study limits the ability to draw definitive conclusions about the presence or absence of newborn neurons, we argue that our data provide a valuable contribution. High-quality human brain specimens suitable for SRT are a rare biological resource, particularly in donors spanning the entire lifespan. Currently, SRT data from human HPC is either limited to adult donors⁶² or contains a single infant donor.³⁸ Our use of spot-based SRT technology on the DG in human donors from infant to elderly allowed us to obtain transcriptome-wide resolution while retaining cytosolic transcripts and spatial accuracy. Generating these data allowed us to deploy spatial enrichment analysis for existing transcriptomic profiles for HPC cell types from mice, macaques, and humans, providing important spatial context.^{21,22,36} We predicted that signatures attributed to imGCs from human donors would localize to the GCL or SGZ, but rather, they are enriched in the CA3&4 (Figure S18). We do not detect the presence of dividing proliferative populations, but our spatial enrichment analysis (Figure S18) and the results from our NMF-based transfer learning analyses (Figures 4 and S19–S21)⁶² support the existence of a GC subpopulation that expresses immature markers through adulthood.⁷⁸ Our data cannot determine if this population persists due to protracted maturation, the expression of immature markers is indicative of a reversion to a more immature cellular state, or this immature cell state represents an alternative endpoint in GC maturation. In support of prolonged maturation in the human DG, maturation trajectories of GCs in macaques are up to six times longer than those in rodents.⁷⁹ Further supporting the ability of GCs to revert their maturation state, chronic fluoxetine administration in mice induces reversion of GCs to immature states.⁸⁰

While we cannot definitively determine the origin of cells that are enriched for imGC pattern nmf26, many genes that define this pattern are enriched in the infant GCL. Some of these nmf26 marker genes, including *POSTN* and *ALDH1A2*, exhibit species-specific expression patterns. *ALDH1A2* and other genes that encode enzymes that synthesize retinoic acid (RA)⁸¹ are enriched in the human GCL but are not highly expressed in the adult mouse DG.⁸² RA promotes synaptic plasticity in DG neurons⁸³ and affects DG neurogenesis in a biphasic manner—depletion reduces neural differentiation and cell survival,^{84,85} while excess amounts reduce neural proliferation.⁸⁶ Given these established roles for *ALDH1A2* and *POSTN* in GC plasticity and development, our data showing the specificity of

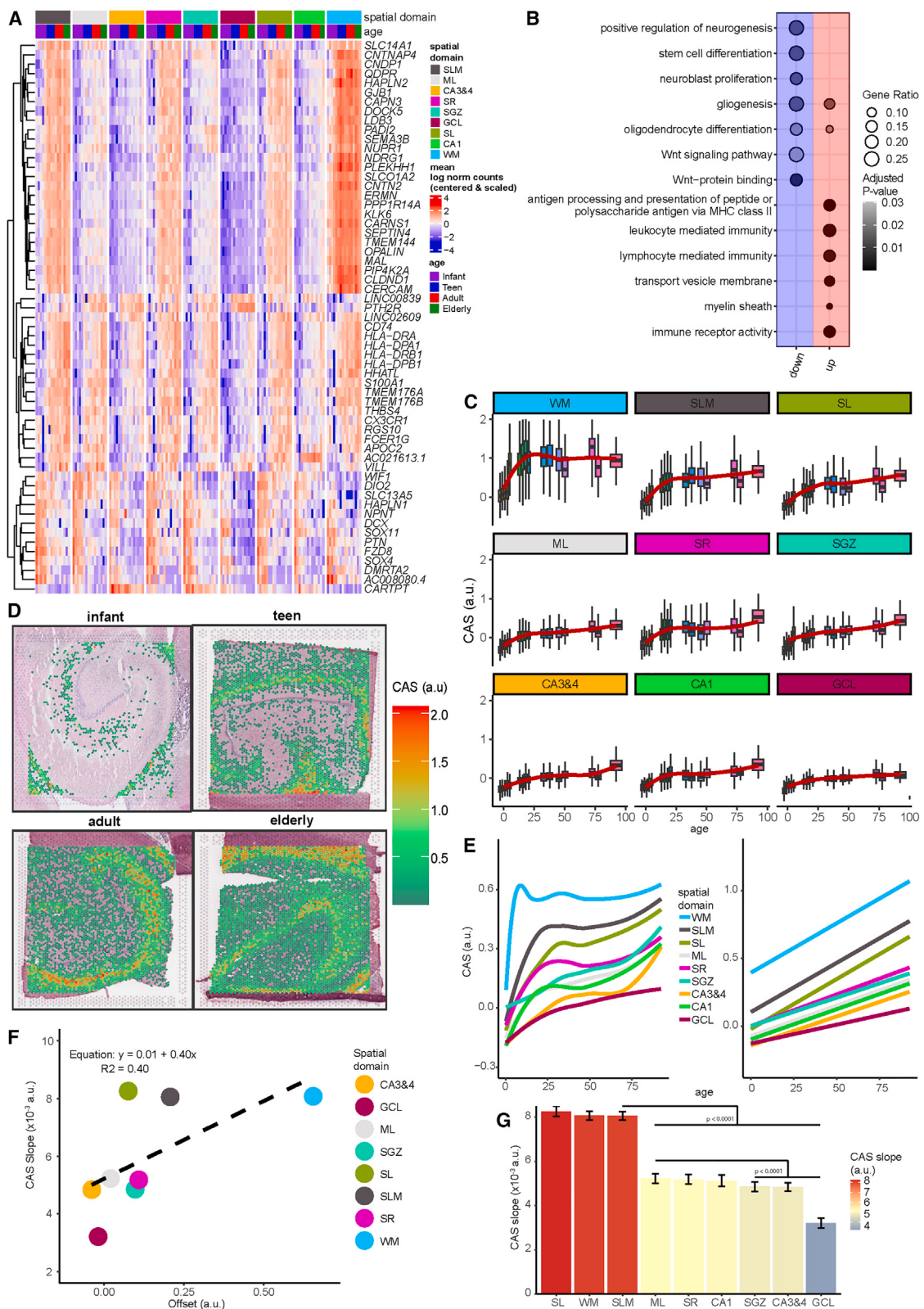
their expression in the human GCL render these genes prime candidates for future studies. Manipulating the expression of these genes in mice postnatally could help determine whether modulating ECM and RA signaling can stimulate proliferation or modulate imGC fate in the DG.

We find increased expression of GABAergic neuron markers, including *GAD1* and *LAMP5*, in the primarily excitatory GCL. *DCX* and *GAD1* co-expression was previously demonstrated in the adult GCL using smFISH and immunohistochemistry.^{38,39} However, *LAMP5*⁺ GABAergic neurons in the GCL have not been reported. Although *LAMP5* protein is localized in axon terminals of GABAergic neurons,⁸⁷ our smFISH data show *LAMP5* transcripts localized in cell bodies. Interestingly, *LAMP5*⁺ excitatory neurons are found in human cortex and basolateral amygdala, and both inhibitory and excitatory *LAMP5*⁺ cells are more abundant in humans than mice.^{88,89} Additional research is needed to determine if the *LAMP5* increase over age is due to increased *LAMP5* transcription in expressor cells, recruitment of previously non-expressing cells to the *LAMP5*⁺ population, or proliferation of a *LAMP5*⁺ population.

We observed the most DEGs in the infant group, followed by the elderly group, suggesting that gene expression changes undergo major shifts over aging. Many elderly enriched genes were associated with neuroinflammation. Because our data leverage the inclusion of cytoplasmic, non-nuclear transcripts, we are able to provide evidence that neuropil-rich regions are preferentially vulnerable to increases in inflammation-related gene expression (Figures 5 and 6). Since microglia show a robust cellular signature of aging in the DG, there is strong interest in evaluating these cells as therapeutic targets for age-associated neurodegeneration and cognitive decline. Our data contribute to existing evidence that microglia accumulate throughout the DG with aging. However, we cannot distinguish if inflammation-associated gene expression is limited to microglia or if other immune cells, such as NK cells, or BBB disruption contribute to these signatures. We observe evidence of BBB disruption (Figures 2D and 5) and increased oxidative stress (Figure 2E), which could drive inflammation and contribute to decreases in neuronal proliferation.^{51,90–92} However, there is conflicting evidence regarding the presence and origin of invasive immune cells in the HPC,^{44,93–95} and although NK cells, T cells, and microglia share some overlapping transcriptional signatures, the extent of overlap in humans is unclear. Additionally, microglial markers also share some overlap with neurons. For example, *CD74* is expressed in activated microglia, but the expression of *CD74* protein has also been detected in neurons,^{96–98} and it may be involved in Alzheimer's disease (AD) pathology.⁹⁶ These findings highlight the importance of analyzing both neuronal and non-neuronal cellular populations across species in aging.

Figure 5. Markers of inflammation are enriched in DG sub-domains in the elderly group

- (A) Enrichment analyses using Fisher's exact tests for predefined gene sets of activated microglial markers. Nomenclature was adopted from each publication: microglial clusters for early_activated_1, early_activated_2, late_activated,⁵⁰ and human microglial cluster 1 (MG1).⁶⁴ Color indicates negative $\log_{10} p$ values, and numbers within the heatmap indicate the odds ratio of enrichment.
- (B) Heatmap of mean \log_2 normalized counts (centered and scaled) of pseudo-bulked DG sub-domains with genes, which satisfy GO accession GO: 0002504. Hierarchical clustering was performed across rows. Columns are organized by domain and age group.
- (C–F) Volcano plots of elderly vs. non-elderly for DG sub-domains: ML (C), GCL (D), SGZ (E), and CA3&4 (F). The x axis is $\log_2 FC$ in expression, and the y axis is negative \log_{10} adjusted p values.



Limitations of the study

The HPC has anatomical and cellular variability, including across the anterior to posterior axis. Axonal projections from the anterior HPC in humans are more similar to the ventral HPC in rodents,^{99–103} and DCX+ cells are more abundant in this region.²⁶ We therefore targeted DG in the anterior-most portion of the human HPC. Postmortem studies have inherent limitations associated with a lack of control over variations of donor background and environmental exposures. To minimize variability, we optimized dissection strategies and ensured that neither the RNA integrity number (RIN) nor the postmortem interval (PMI) differed across donors or age groups (Figure S10; Table S1). Despite our relatively small sample size (5 infant, 4 teen, 4 adult, and 3 elderly donors), the inclusion of multiple infant and elderly samples in our cohort maximizes the potential for detecting differential gene expression patterns across the human lifespan. However, the small sample size likely limits statistical power to identify age-associated DEGs across groups, and thus, our results may be biased toward more extreme differences or may fail to detect subtle changes.

Given the non-uniform cellular distribution of the HPC, SRT is useful to understand gene expression across cell types. However, given their relatively large size (55 μm diameter), Visium spots may contain multiple cell types, and cell density across spots can be heterogeneous. Thus, age-associated statistics, including CASs, may be biased by changes in cell composition or abundance and, hence, do not represent a truly cell-independent signature of aging. Unfortunately, our data lacked nuclei segmentation for some samples, which precluded the inclusion of nuclei density as a covariate in CAS calculations. Newer sequencing technologies, including cell-based *in situ* sequencing of *a priori* identified gene panels and higher resolution spot-based methods with transcriptome-wide capabilities, can be deployed to validate our results and will extend our understanding of gene expression changes in the HPC over the lifespan. Despite these limitations, our study, which includes donors across the lifespan and extranuclear transcripts with spatial-domain-level specificity, is a valuable resource that provides critical insight into species-specific cellular mechanisms of HPC development and age-associated changes in HPC function.

RESOURCE AVAILABILITY

Lead contact

Further information and requests for resources not provided below should be directed to the lead contact, Stephanie C. Page (stephanie.page@libd.org).

Figure 6. Widespread HPC aging signature identifies regions of local tissue that change more with age

- (A) Heatmap of the mean log₂ normalized counts (centered and scaled) for widespread aging signature gene set. Hierarchical clustering was performed across rows. Columns are organized by spatial domain and age.
- (B) Dot plot for GO terms from aging signature gene set, faceted by down- and upregulation columns colored blue and red, respectively; dot size represents the gene ratio, and black gradient represents adjusted *p* values.
- (C) Boxplots of CAS (arbitrary units) of gene expression spots vs. age, faceted by spatial domain and fitted with local regression line.
- (D) Data visualization of spots from one representative sample per age group (infant-Br8533, teen-Br1412, adult-Br3942, and elderly-Br5242). Spots are colored by CAS (arbitrary units, spots with CAS = 0 omitted for visualization).
- (E) CAS trajectories of all spatial domains vs. age approximated via local (left) and linear (right) regression.
- (F) Offset from infant of linear fit and slope from linear modeling of CASs across all spots.
- (G) CAS slope of linear approximations in (E), colored by slope, for each spatial domain. Mean ± 95% confidence intervals. Adjusted *p* values were derived from two-sided Tukey's honestly significant difference (HSD) test.

Materials availability

This study did not generate new reagents or materials.

Data and code availability

- Data: all data are publicly available as described in the [key resources table](#). All FASTQ files are available through SRA. Raw data provided through Zenodo include all FASTQ files and raw image files.¹⁰⁴ The processed data available through Zenodo include two *spe* objects: (1) raw, untransformed feature counts and (2) normalized log₂-transformed feature counts, batch correction, unsupervised spatial clustering, and cell type deconvolution.¹⁰⁴
- Code: the code for this project is publicly available and listed in the [key resources table](#).¹⁰⁵ Analyses were performed using R v.4.2.1 with Bioconductor v.3.15.2. cell2location v.0.1.3 was employed via the reticulate R package v.1.28.
- Additional information: an interactive web-based data portal is available to interactively plot genes of interest and explore DEGs across spatial domains (https://libd.shinyapps.io/Lifespan_DG/).¹⁰⁶ Any additional information required to reanalyze the data reported in this paper is available from the [lead contact](#) upon request.

ACKNOWLEDGMENTS

Portions of some of the figures were generated with [BioRender.com](#). We thank the LIBD neuropathology team, particularly James Tooke and Amy Deep-Soboslay, for curating the brain samples and assisting with tissue dissections. We thank the staff and physicians at the brain donation sites and are grateful for the generosity of the brain donors and their families, without whom this work would not be possible. We thank Andrew E. Jaffe, Daniel R. Weinberger, and members of the LIBD spatial team for helpful feedback on the manuscript. Finally, we thank the families of Connie and Steve Lieber and Milton and Tamar Maltz for their generous support. Funding for this project was provided by NIMH (U01MH122849 to K.M.), NIA (R21AG083328 to S.C.P. and S.C.H.), and the Lieber Institute for Brain Development.

AUTHOR CONTRIBUTIONS

Conceptualization, A.D.R., K.M., and S.C.P.; data curation, A.D.R., H.R.D., and S.C.P.; formal analysis, A.D.R., M.T., H.R.D., E.D.N., and S.C.H.; investigation, A.D.R., M.T., H.R.D., A.R.P., EAP, E.D.N., J.R.T., and S.C.P.; methodology, A.D.R., S.C.H., E.D.N., and J.R.T.; validation, A.D.R. and A.R.P.; resources, J.E.K. and T.M.H.; software, A.D.R., H.R.D., and R.A.M.; visualization, A.D.R., M.T., A.R.P., and S.C.P.; project administration, K.R.M., L.C.-T., K.M., S.C.H., and S.C.P.; supervision, K.R.M., K.M., S.C.H., and S.C.P.; funding acquisition, K.M., S.C.H., and S.C.P.; writing – original draft, A.D.R.; writing – review & editing, A.D.R., K.M., S.C.H., and S.C.P.

DECLARATION OF INTERESTS

E.D.N. is now employed by GlaxoSmithKlein, which is unrelated to the contents of this manuscript. J.E.K. is a consultant on a data monitoring committee for an antipsychotic drug trial for Merck.

STAR★METHODS

Detailed methods are provided in the online version of this paper and include the following:

- KEY RESOURCES TABLE
- EXPERIMENTAL MODEL AND STUDY PARTICIPANT DETAILS
- METHOD DETAILS
 - Tissue processing and quality control
 - Visium data generation
 - Single-molecule fluorescent *in situ* hybridization (smFISH) and imaging
- QUANTIFICATION AND STATISTICAL ANALYSIS
 - Visium raw data processing
 - Visium-H&E image segmentation and processing
 - Spot-level data processing
 - Spatial domain detection and annotation
 - Spatial domain comparison
 - Spatial domain-level processing
 - Spatial domain-level gene modeling of age groups
 - Functional enrichment analyses
 - Transfer learning of NMF patterns
 - Spot-level deconvolution of cell types
 - Aging gene signature generation and score calculation
 - Reproducibility
- ADDITIONAL RESOURCES

SUPPLEMENTAL INFORMATION

Supplemental information can be found online at <https://doi.org/10.1016/j.celrep.2025.115300>.

Received: May 24, 2024

Revised: September 19, 2024

Accepted: January 21, 2025

Published: February 19, 2025

REFERENCES

1. Hainmueller, T., and Bartos, M. (2020). Dentate gyrus circuits for encoding, retrieval and discrimination of episodic memories. *Nat. Rev. Neurosci.* 21, 153–168. <https://doi.org/10.1038/s41583-019-0260-z>.
2. Kesner, R.P. (2018). An analysis of dentate gyrus function (an update). *Behav. Brain Res.* 354, 84–91. <https://doi.org/10.1016/j.bbr.2017.07.033>.
3. Xavier, G.F., and Costa, V.C.I. (2009). Dentate gyrus and spatial behaviour. *Prog. Neuro-Psychopharmacol. Biol. Psychiatry* 33, 762–773. <https://doi.org/10.1016/j.pnpbp.2009.03.036>.
4. Zou, D., Chen, L., Deng, D., Jiang, D., Dong, F., McSweeney, C., Zhou, Y., Liu, L., Chen, G., Wu, Y., and Mao, Y. (2016). DREADD in parvalbumin interneurons of the dentate gyrus modulates anxiety, social interaction and memory extinction. *Curr. Mol. Med.* 16, 91–102. <https://doi.org/10.2174/1566524016666151222150024>.
5. Chen, S., Chen, F., Amin, N., Ren, Q., Ye, S., Hu, Z., Tan, X., Jiang, M., and Fang, M. (2022). Defects of parvalbumin-positive interneurons in the ventral dentate gyrus region are implicated depression-like behavior in mice. *Brain Behav. Immun.* 99, 27–42. <https://doi.org/10.1016/j.bbi.2021.09.013>.
6. Karayol, R., Medrihan, L., Warner-Schmidt, J.L., Fait, B.W., Rao, M.N., Holzner, E.B., Greengard, P., Heintz, N., and Schmidt, E.F. (2021). Serotonin receptor 4 in the hippocampus modulates mood and anxiety. *Mol. Psychiatr.* 26, 2334–2349. <https://doi.org/10.1038/s41380-020-00994-y>.
7. Schomaker, J., Baumann, V., and Ruitenberg, M.F.L. (2022). Effects of exploring a novel environment on memory across the lifespan. *Sci. Rep.* 12, 16631. <https://doi.org/10.1038/s41598-022-20562-4>.
8. Lavenex, P., and Banta Lavenex, P. (2013). Building hippocampal circuits to learn and remember: insights into the development of human memory. *Behav. Brain. Res.* 254, 8–21. <https://doi.org/10.1016/j.bbr.2013.02.007>.
9. Ghetti, S., and Bunge, S.A. (2012). Neural changes underlying the development of episodic memory during middle childhood. *Dev. Cogn. Neurosci.* 2, 381–395. <https://doi.org/10.1016/j.dcn.2012.05.002>.
10. Petersen, R.C. (2016). Mild Cognitive Impairment. *Continuum* 22, 404–418. <https://doi.org/10.1212/CON.0000000000000313>.
11. Plassman, B.L., Langa, K.M., Fisher, G.G., Heeringa, S.G., Weir, D.R., Ofstedal, M.B., Burke, J.R., Hurd, M.D., Potter, G.G., Rodgers, W.L., et al. (2008). Prevalence of cognitive impairment without dementia in the United States. *Ann. Intern. Med.* 148, 427–434.
12. Boyle, P.A., Wilson, R.S., Yu, L., Barr, A.M., Honer, W.G., Schneider, J.A., and Bennett, D.A. (2013). Much of late life cognitive decline is not due to common neurodegenerative pathologies. *Ann. Neurol.* 74, 478–489. <https://doi.org/10.1002/ana.23964>.
13. Watson, R., Colloby, S.J., Blamire, A.M., and O'Brien, J.T. (2016). Subcortical volume changes in dementia with Lewy bodies and Alzheimer's disease. A comparison with healthy aging. *Int. Psychogeriatr.* 28, 529–536. <https://doi.org/10.1017/S1041610215001805>.
14. Dickerson, B.C., Salat, D.H., Greve, D.N., Chua, E.F., Rand-Giovannetti, E., Rentz, D.M., Bertram, L., Mullin, K., Tanzi, R.E., Blacker, D., et al. (2005). Increased hippocampal activation in mild cognitive impairment compared to normal aging and AD. *Neurology* 65, 404–411. <https://doi.org/10.1212/01.wnl.0000171450.97464.49>.
15. Amaral, D.G., Scharfman, H.E., and Lavenex, P. (2007). The dentate gyrus: fundamental neuroanatomical organization (dentate gyrus for dummies). *Prog. Brain. Res.* 163, 3–22. [https://doi.org/10.1016/S0079-6123\(07\)63001-5](https://doi.org/10.1016/S0079-6123(07)63001-5).
16. Seress, L. (2007). Comparative anatomy of the hippocampal dentate gyrus in adult and developing rodents, non-human primates and humans. In *The Dentate Gyrus: A Comprehensive Guide to Structure, Function, and Clinical Implications Progress in Brain Research*, H.E. Scharfman, ed. (Elsevier), pp. 23–798. [https://doi.org/10.1016/S0079-6123\(07\)63002-7](https://doi.org/10.1016/S0079-6123(07)63002-7).
17. Borzello, M., Ramirez, S., Treves, A., Lee, I., Scharfman, H., Stark, C., Knierim, J.J., and Rangel, L.M. (2023). Assessments of dentate gyrus function: discoveries and debates. *Nat. Rev. Neurosci.* 24, 502–517. <https://doi.org/10.1038/s41583-023-00710-z>.
18. Toda, T., Parylak, S.L., Linker, S.B., and Gage, F.H. (2019). The role of adult hippocampal neurogenesis in brain health and disease. *Mol. Psychiatr.* 24, 67–87. <https://doi.org/10.1038/s41380-018-0036-2>.
19. Snyder, J.S. (2019). Recalibrating the relevance of adult neurogenesis. *Trends Neurosci.* 42, 164–178. <https://doi.org/10.1016/j.tins.2018.12.001>.
20. Simard, S., Matosin, N., and Mechawar, N. (2024). Adult hippocampal neurogenesis in the human brain: updates, challenges, and perspectives. *Neuroscientist*, 10738584241252581. <https://doi.org/10.1177/10738584241252581>.
21. Hochgerner, H., Zeisel, A., Lönnérberg, P., and Linnarsson, S. (2018). Conserved properties of dentate gyrus neurogenesis across postnatal development revealed by single-cell RNA sequencing. *Nat. Neurosci.* 21, 290–299. <https://doi.org/10.1038/s41593-017-0056-2>.
22. Hao, Z.-Z., Wei, J.-R., Xiao, D., Liu, R., Xu, N., Tang, L., Huang, M., Shen, Y., Xing, C., Huang, W., et al. (2022). Single-cell transcriptomics of adult macaque hippocampus reveals neural precursor cell populations. *Nat. Neurosci.* 25, 805–817. <https://doi.org/10.1038/s41593-022-01073-x>.
23. Eriksson, P.S., Perfilieva, E., Björk-Eriksson, T., Alborn, A.M., Nordborg, C., Peterson, D.A., and Gage, F.H. (1998). Neurogenesis in the adult human hippocampus. *Nat. Med.* 4, 1313–1317. <https://doi.org/10.1038/3305>.
24. Knotz, R., Singec, I., Ditter, M., Pantazis, G., Capetian, P., Meyer, R.P., Horvat, V., Volk, B., and Kempermann, G. (2010). Murine features of neurogenesis in the human hippocampus across the lifespan from 0 to 100

- years. *PLoS One* 5, e8809. <https://doi.org/10.1371/journal.pone.0008809>.
25. Dennis, C.V., Suh, L.S., Rodriguez, M.L., Kril, J.J., and Sutherland, G.T. (2016). Human adult neurogenesis across the ages: An immunohistochemical study. *Neuropathol. Appl. Neurobiol.* 42, 621–638. <https://doi.org/10.1111/nan.12337>.
 26. Boldrini, M., Fulmore, C.A., Tartt, A.N., Simeon, L.R., Pavlova, I., Po-poska, V., Rosoklja, G.B., Stankov, A., Arango, V., Dwork, A.J., et al. (2018). Human Hippocampal Neurogenesis Persists throughout Aging. *Cell Stem Cell* 22, 589–599.e5. <https://doi.org/10.1016/j.stem.2018.03.015>.
 27. Moreno-Jiménez, E.P., Flor-García, M., Terreros-Roncal, J., Rábano, A., Cafini, F., Pallas-Bazarrá, N., Ávila, J., and Llorens-Martín, M. (2019). Adult hippocampal neurogenesis is abundant in neurologically healthy subjects and drops sharply in patients with Alzheimer's disease. *Nature* 55, 554–560.
 28. Tobin, M.K., Musaraca, K., Disouky, A., Shetti, A., Bheri, A., Honer, W.G., Kim, N., Dawe, R.J., Bennett, D.A., Arfanakis, K., and Lazarov, O. (2019). Human hippocampal neurogenesis persists in aged adults and Alzheimer's disease patients. *Cell Stem Cell* 24, 974–982.e3. <https://doi.org/10.1016/j.stem.2019.05.003>.
 29. Seki, T., Hori, T., Miyata, H., Maehara, M., and Namba, T. (2019). Analysis of proliferating neuronal progenitors and immature neurons in the human hippocampus surgically removed from control and epileptic patients. *Sci. Rep.* 9, 18194. <https://doi.org/10.1038/s41598-019-54684-z>.
 30. Terreros-Roncal, J., Moreno-Jiménez, E.P., Flor-García, M., Rodríguez-Moreno, C.B., Trinchero, M.F., Cafini, F., Rábano, A., and Llorens-Martín, M. (2021). Impact of neurodegenerative diseases on human adult hippocampal neurogenesis. *Science* 374, 1106–1113. <https://doi.org/10.1126/science.abl5163>.
 31. Ammoothumkandy, A., Ravina, K., Wolsey, V., Tartt, A.N., Yu, P.-N., Corona, L., Zhang, N., Nune, G., Kalayjian, L., Mann, J.J., et al. (2022). Altered adult neurogenesis and gliogenesis in patients with mesial temporal lobe epilepsy. *Nat. Neurosci.* 25, 493–503. <https://doi.org/10.1038/s41593-022-01044-2>.
 32. Sorrells, S.F., Paredes, M.F., Zhang, Z., Kang, G., Pastor-Alonso, O., Biagiotti, S., Page, C.E., Sandoval, K., Knox, A., Connolly, A., et al. (2021). Positive controls in adults and children support that very few, if any, new neurons are born in the adult human hippocampus. *J. Neurosci.* 41, 2554–2565. <https://doi.org/10.1523/JNEUROSCI.0676-20.2020>.
 33. Sorrells, S.F., Paredes, M.F., Cebrán-Silla, A., Sandoval, K., Qi, D., Kelley, K.W., James, D., Mayer, S., Chang, J., Auguste, K.I., et al. (2018). Human hippocampal neurogenesis drops sharply in children to undetectable levels in adults. *Nature* 555, 377–381. <https://doi.org/10.1038/nature25975>.
 34. Cipriani, S., Ferrer, I., Aronica, E., Kovacs, G.G., Verney, C., Nardelli, J., Khung, S., Delezoide, A.-L., Milenkovic, I., Rasika, S., et al. (2018). Hippocampal radial glial subtypes and their neurogenic potential in human fetuses and healthy and Alzheimer's disease adults. *Cerebr. Cortex* 28, 2458–2478. <https://doi.org/10.1093/cercor/bhy096>.
 35. Lu, Z., Zhang, M., Lee, J., Sziraki, A., Anderson, S., Zhang, Z., Xu, Z., Jiang, W., Ge, S., Nelson, P.T., et al. (2023). Tracking cell-type-specific temporal dynamics in human and mouse brains. *Cell* 186, 4345–4364.e24. <https://doi.org/10.1016/j.cell.2023.08.042>.
 36. Zhou, Y., Su, Y., Li, S., Kennedy, B.C., Zhang, D.Y., Bond, A.M., Sun, Y., Jacob, F., Lu, L., Hu, P., et al. (2022). Molecular landscapes of human hippocampal immature neurons across lifespan. *Nature* 607, 527–533. <https://doi.org/10.1038/s41586-022-04912-w>.
 37. Yao, J., Dai, S., Zhu, R., Tan, J., Zhao, Q., Yin, Y., Sun, J., Du, X., Ge, L., Xu, J., et al. (2024). Deciphering molecular heterogeneity and dynamics of human hippocampal neural stem cells at different ages and injury states. *Elife* 12, RP89507. <https://doi.org/10.7554/elife.89507>.
 38. Simard, S., Rahimian, R., Davoli, M.A., Théberge, S., Matosin, N., Tur-ecki, G., Nagy, C., and Mechawar, N. (2024). Spatial transcriptomic analysis of adult hippocampal neurogenesis in the human brain. *J. Psychiatry Neurosci.* 49, E319–E333. <https://doi.org/10.1503/jpn.240026>.
 39. Franjic, D., Skarica, M., Ma, S., Arellano, J.I., Tebberkamp, A.T.N., Choi, J., Xu, C., Li, Q., Morozov, Y.M., Andrijevic, D., et al. (2022). Transcriptomic taxonomy and neurogenic trajectories of adult human, macaque, and pig hippocampal and entorhinal cells. *Neuron* 110, 452–469.e14. <https://doi.org/10.1016/j.neuron.2021.10.036>.
 40. Ayhan, F., Kulkarni, A., Berto, S., Sivaprakasam, K., Douglas, C., Lega, B.C., and Konopka, G. (2021). Resolving cellular and molecular diversity along the hippocampal anterior-to-posterior axis in humans. *Neuron* 109, 2091–2105.e6. <https://doi.org/10.1016/j.neuron.2021.05.003>.
 41. Jaffe, A.E., Hoeppner, D.J., Saito, T., Blanpain, L., Ukaigwe, J., Burke, E.E., Collado-Torres, L., Tao, R., Tajinda, K., Maynard, K.R., et al. (2020). Profiling gene expression in the human dentate gyrus granule cell layer reveals insights into schizophrenia and its genetic risk. *Nat. Neurosci.* 23, 510–519. <https://doi.org/10.1038/s41593-020-0604-z>.
 42. Lana, D., Ugolini, F., Nosi, D., Wenk, G.L., and Giovannini, M.G. (2021). The emerging role of the interplay among astrocytes, microglia, and neurons in the hippocampus in health and disease. *Front. Aging Neurosci.* 13, 651973. <https://doi.org/10.3389/fnagi.2021.651973>.
 43. Montagne, A., Barnes, S.R., Sweeney, M.D., Halliday, M.R., Sagare, A.P., Zhao, Z., Toga, A.W., Jacobs, R.E., Liu, C.Y., Amezcuia, L., et al. (2015). Blood-brain barrier breakdown in the aging human hippocampus. *Neuron* 85, 296–302. <https://doi.org/10.1016/j.neuron.2014.12.032>.
 44. Jin, W.-N., Shi, K., He, W., Sun, J.-H., Van Kaer, L., Shi, F.-D., and Liu, Q. (2021). Neuroblast senescence in the aged brain augments natural killer cell cytotoxicity leading to impaired neurogenesis and cognition. *Nat. Neurosci.* 24, 61–73. <https://doi.org/10.1038/s41593-020-00745-w>.
 45. Menet, V., Ribotta, M.G.Y., Sandillon, F., and Privat, A. (2000). GFAP null astrocytes are a favorable substrate for neuronal survival and neurite growth. *Glia* 31, 267–272.
 46. Larsson, A., Wilhelmsson, U., Pekna, M., and Pekny, M. (2004). Increased cell proliferation and neurogenesis in the hippocampal dentate gyrus of old GFAP(-/-)Vim(-/-) mice. *Neurochem. Res.* 29, 2069–2073. <https://doi.org/10.1007/s11064-004-6880-2>.
 47. Barrientos, R.M., Kitt, M.M., Watkins, L.R., and Maier, S.F. (2015). Neuroinflammation in the normal aging hippocampus. *Neuroscience* 309, 84–99. <https://doi.org/10.1016/j.neuroscience.2015.03.007>.
 48. Liddelow, S.A., Guttenplan, K.A., Clarke, L.E., Bennett, F.C., Bohlen, C.J., Schirmer, L., Bennett, M.L., Münch, A.E., Chung, W.-S., Peterson, T.C., et al. (2017). Neurotoxic reactive astrocytes are induced by activated microglia. *Nature* 541, 481–487. <https://doi.org/10.1038/nature21029>.
 49. Clarke, L.E., Liddelow, S.A., Chakraborty, C., Münch, A.E., Heiman, M., and Barres, B.A. (2018). Normal aging induces A1-like astrocyte reactivity. *Proc. Natl. Acad. Sci. USA* 115, E1896–E1905. <https://doi.org/10.1073/pnas.1800165115>.
 50. Mathys, H., Adaikan, C., Gao, F., Young, J.Z., Manet, E., Hemberg, M., De Jager, P.L., Ransohoff, R.M., Regev, A., and Tsai, L.-H. (2017). Temporal Tracking of Microglia Activation in Neurodegeneration at Single-Cell Resolution. *Cell Rep.* 21, 366–380. <https://doi.org/10.1016/j.celrep.2017.09.039>.
 51. Maciel-Barón, L.Á., Moreno-Blas, D., Morales-Rosales, S.L., González-Puertos, V.Y., López-Díazguerrero, N.E., Torres, C., Castro-Obregón, S., and Königsberg, M. (2018). Cellular senescence, neurological function, and redox state. *Antioxid. Redox. Signal.* 28, 1704–1723. <https://doi.org/10.1089/ars.2017.7112>.
 52. Angelova, D.M., and Brown, D.R. (2019). Microglia and the aging brain: are senescent microglia the key to neurodegeneration? *J. Neurochem.* 151, 676–688. <https://doi.org/10.1111/jnc.14860>.
 53. Neumann, P., Lenz, D.E., Streit, W.J., and Bechmann, I. (2023). Is microglial dystrophy a form of cellular senescence? An analysis of senescence markers in the aged human brain. *Glia* 71, 377–390. <https://doi.org/10.1002/glia.24282>.

54. Galatro, T.F., Holtman, I.R., Lerario, A.M., Vainchtein, I.D., Brouwer, N., Sola, P.R., Veras, M.M., Pereira, T.F., Leite, R.E.P., Möller, T., et al. (2017). Transcriptomic analysis of purified human cortical microglia reveals age-associated changes. *Nat. Neurosci.* **20**, 1162–1171. <https://doi.org/10.1038/nn.4597>.
55. Zhao, E., Stone, M.R., Ren, X., Guenthoer, J., Smythe, K.S., Pulliam, T., Williams, S.R., Utyngco, C.R., Taylor, S.E.B., Nghiem, P., et al. (2021). Spatial transcriptomics at subspot resolution with BayesSpace. *Nat. Biotechnol.* **39**, 1375–1384. <https://doi.org/10.1038/s41587-021-00935-2>.
56. Huuki-Myers, L.A., Spangler, A., Eagles, N.J., Montgomery, K.D., Kwon, S.H., Guo, B., Grant-Peters, M., Divecha, H.R., Tippani, M., Sriworarat, C., et al. (2024). A data-driven single-cell and spatial transcriptomic map of the human prefrontal cortex. *Science* **384**, eadh1938. <https://doi.org/10.1126/science.adh1938>.
57. Collado-Torres, L., Burke, E.E., Peterson, A., Shin, J., Straub, R.E., Rajpurkar, A., Semick, S.A., Ulrich, W.S., BrainSeq Consortium; Price, A.J., and Valencia, C. (2019). Regional Heterogeneity in Gene Expression, Regulation, and Coherence in the Frontal Cortex and Hippocampus across Development and Schizophrenia. *Neuron* **103**, 203–216.e8. <https://doi.org/10.1016/j.neuron.2019.05.013>.
58. Tzilivaki, A., Tukker, J.J., Maier, N., Poirazi, P., Sammons, R.P., and Schmitz, D. (2023). Hippocampal GABAergic interneurons and memory. *Neuron* **111**, 3154–3175. <https://doi.org/10.1016/j.neuron.2023.06.016>.
59. Ma, S.-M., Chen, L.-X., Lin, Y.-F., Yan, H., Lv, J.-W., Xiong, M., Li, J., Cheng, G.-Q., Yang, Y., Qiu, Z.-L., and Zhou, W.H. (2015). Periostin Promotes Neural Stem Cell Proliferation and Differentiation following Hypoxic-Ischemic Injury. *PLoS One* **10**, e0123585. <https://doi.org/10.1371/journal.pone.0123585>.
60. Zhou, Q.-J., Liu, X., Zhang, L., Wang, R., Yin, T., Li, X., Li, G., He, Y., Ding, Z., Ma, P., et al. (2022). A single-nucleus transcriptomic atlas of the dog hippocampus reveals the potential relationship between specific cell types and domestication. *Natl. Sci. Rev.* **9**, nwac147. <https://doi.org/10.1093/nsr/nwac147>.
61. Stein-O'Brien, G.L., Clark, B.S., Sherman, T., Zibetti, C., Hu, Q., Sealfon, R., Liu, S., Qian, J., Colantuoni, C., Blackshaw, S., et al. (2019). Decomposing Cell Identity for Transfer Learning across Cellular Measurements, Platforms, Tissues, and Species. *Cell Syst.* **8**, 395–411.e8. <https://doi.org/10.1016/j.cels.2019.04.004>.
62. Thompson, J.R., Nelson, E.D., Tippani, M., Ramnauth, A.D., Divecha, H.R., Miller, R.A., Eagles, N.J., Pattie, E.A., Kwon, S.H., Bach, S.V., et al. (2024). An integrated single-nucleus and spatial transcriptomics atlas reveals the molecular landscape of the human hippocampus. Preprint at bioRxiv, 2024.04.26.590643. <https://doi.org/10.1101/2024.04.26.590643>.
63. Chen, Y.-J., Deng, S.-M., Chen, H.-W., Tsao, C.-H., Chen, W.-T., Cheng, S.-J., Huang, H.-S., Tan, B.-C.-M., Matzuk, M.M., Flint, J., and Huang, G.J. (2021). Follistatin mediates learning and synaptic plasticity via regulation of Asic4 expression in the hippocampus. *Proc. Natl. Acad. Sci. USA* **118**, e2109040118. <https://doi.org/10.1073/pnas.2109040118>.
64. Su, Y., Zhou, Y., Bennett, M.L., Li, S., Carceles-Cordon, M., Lu, L., Huh, S., Jimenez-Cyrus, D., Kennedy, B.C., Kessler, S.K., et al. (2022). A single-cell transcriptome atlas of glial diversity in the human hippocampus across the postnatal lifespan. *Cell Stem Cell* **29**, 1594–1610.e8. <https://doi.org/10.1016/j.stem.2022.09.010>.
65. Srpan, K., Ambrose, A., Karampatzakis, A., Saeed, M., Cartwright, A.N.R., Guideval, K., De Matos, G.D.S.C., Önfelt, B., and Davis, D.M. (2018). Shedding of CD16 disassembles the NK cell immune synapse and boosts serial engagement of target cells. *J. Cell. Biol.* **217**, 3267–3283. <https://doi.org/10.1083/jcb.201712085>.
66. Warren, H.S., and Kinnear, B.F. (1999). Quantitative analysis of the effect of CD16 ligation on human NK cell proliferation. *J. Immunol.* **162**, 735–742.
67. Kleshchevnikov, V., Shmatko, A., Dann, E., Aivazidis, A., King, H.W., Li, T., Elmentaita, R., Lomakin, A., Kedlian, V., Gayoso, A., et al. (2022). Cell2location maps fine-grained cell types in spatial transcriptomics. *Nat. Biotechnol.* **40**, 661–671. <https://doi.org/10.1038/s41587-021-01139-4>.
68. Hahn, O., Foltz, A.G., Atkins, M., Kedir, B., Moran-Losada, P., Guldner, I.H., Munson, C., Kern, F., Pállovics, R., Lu, N., et al. (2023). Atlas of the aging mouse brain reveals white matter as vulnerable foci. *Cellule* **186**, 4117–4133.e22. <https://doi.org/10.1016/j.cell.2023.07.027>.
69. DeTomaso, D., Jones, M.G., Subramaniam, M., Ashuach, T., Ye, C.J., and Yosef, N. (2019). Functional interpretation of single cell similarity maps. *Nat. Commun.* **10**, 4376. <https://doi.org/10.1038/s41467-019-12235-0>.
70. Gríñan-Ferré, C., Pérez-Cáceres, D., Gutiérrez-Zetina, S.M., Camins, A., Palomera-Avalos, V., Ortúño-Sahagún, D., Rodrigo, M.T., and Pallás, M. (2016). Environmental Enrichment Improves Behavior, Cognition, and Brain Functional Markers in Young Senescence-Accelerated Prone Mice (SAMP8). *Mol. Neurobiol.* **53**, 2435–2450. <https://doi.org/10.1007/s12035-015-9210-6>.
71. Li, H., Xu, L., Jiang, W., Qiu, X., Xu, H., Zhu, F., Hu, Y., Liang, S., Cai, C., Qiu, W., et al. (2023). Pleiotrophin ameliorates age-induced adult hippocampal neurogenesis decline and cognitive dysfunction. *Cell Rep.* **42**, 113022. <https://doi.org/10.1016/j.celrep.2023.113022>.
72. Ramsaran, A.I., Wang, Y., Golbabaei, A., Aleshin, S., de Snoo, M.L., Yeung, B.-R.A., Rashid, A.J., Awasthi, A., Lau, J., Tran, L.M., et al. (2023). A shift in the mechanisms controlling hippocampal engram formation during brain maturation. *Science* **380**, 543–551. <https://doi.org/10.1126/science.adc6530>.
73. Matsunaga, E., Nambu, S., Oka, M., Tanaka, M., Taoka, M., and Iriki, A. (2015). Periostin, a neurite outgrowth-promoting factor, is expressed at high levels in the primate cerebral cortex. *Dev. Growth. Differ.* **57**, 200–208. <https://doi.org/10.1111/dgd.12194>.
74. Moreno-Jiménez, E.P., Terreros-Roncal, J., Flor-García, M., Rábano, A., and Llorens-Martín, M. (2021). Evidences for adult hippocampal neurogenesis in humans. *J. Neurosci.* **41**, 2541–2553. <https://doi.org/10.1523/JNEUROSCI.0675-20.2020>.
75. Kohen, R., Dobra, A., Tracy, J.H., and Haugen, E. (2014). Transcriptome profiling of human hippocampus dentate gyrus granule cells in mental illness. *Transl. Psychiatry* **4**, e366. <https://doi.org/10.1038/tp.2014.9>.
76. Siletti, K., Hodge, R., Mossi Albiach, A., Lee, K.W., Ding, S.-L., Hu, L., Lönnérberg, P., Bakken, T., Casper, T., Clark, M., et al. (2023). Transcriptomic diversity of cell types across the adult human brain. *Science* **382**, eadd7046. <https://doi.org/10.1126/science.add7046>.
77. Tosoni, G., Ayyildiz, D., Bryois, J., Macnair, W., Fitzsimons, C.P., Lucas-sen, P.J., and Salta, E. (2023). Mapping human adult hippocampal neurogenesis with single-cell transcriptomics: Reconciling controversy or fueling the debate? *Neuron* **111**, 1714–1731.e3. <https://doi.org/10.1016/j.neuron.2023.03.010>.
78. Seki, T. (2020). Understanding the Real State of Human Adult Hippocampal Neurogenesis From Studies of Rodents and Non-human Primates. *Front. Neurosci.* **14**, 839. <https://doi.org/10.3389/fnins.2020.00839>.
79. Kohler, S.J., Williams, N.I., Stanton, G.B., Cameron, J.L., and Greenough, W.T. (2011). Maturation time of new granule cells in the dentate gyrus of adult macaque monkeys exceeds six months. *Proc. Natl. Acad. Sci. USA* **108**, 10326–10331. <https://doi.org/10.1073/pnas.1017099108>.
80. Kobayashi, K., Ikeda, Y., Sakai, A., Yamasaki, N., Haneda, E., Miyakawa, T., and Suzuki, H. (2010). Reversal of hippocampal neuronal maturation by serotonergic antidepressants. *Proc. Natl. Acad. Sci. USA* **107**, 8434–8439. <https://doi.org/10.1073/pnas.0912690107>.
81. Mey, J., and McCaffery, P. (2004). Retinoic acid signaling in the nervous system of adult vertebrates. *Neuroscientist* **10**, 409–421. <https://doi.org/10.1177/1073858404263520>.
82. Fragoso, Y.D., Shearer, K.D., Sementilli, A., de Carvalho, L.V., and McCaffery, P.J. (2012). High expression of retinoic acid receptors and

- synthetic enzymes in the human hippocampus. *Brain Struct. Funct.* 217, 473–483. <https://doi.org/10.1007/s00429-011-0359-0>.
83. Lenz, M., Eichler, A., Kruse, P., Muellerleile, J., Deller, T., Jedlicka, P., and Vlachos, A. (2021). All-trans retinoic acid induces synaptopodin-dependent metaplasticity in mouse dentate granule cells. *Elife* 10, e71983. <https://doi.org/10.7554/eLife.71983>.
 84. Jacobs, S., Lie, D.C., DeCicco, K.L., Shi, Y., DeLuca, L.M., Gage, F.H., and Evans, R.M. (2006). Retinoic acid is required early during adult neurogenesis in the dentate gyrus. *Proc. Natl. Acad. Sci. USA* 103, 3902–3907. <https://doi.org/10.1073/pnas.0511294103>.
 85. Como, C.N., O'Rourke, R., Winkler, C., Mitchell, D., Tran, L.N., Lorberbaum, D., Sussel, L., Franco, S.J., and Siegenthaler, J.A. (2024). Meningeal-derived Retinoic Acid Regulates Neurogenesis via Suppression of Notch and Sox2. Preprint at BioRxiv. <https://doi.org/10.1101/2024.04.05.588348>.
 86. Crandall, J., Sakai, Y., Zhang, J., Koul, O., Mineur, Y., Crusio, W.E., and McCaffery, P. (2004). 13-cis-retinoic acid suppresses hippocampal cell division and hippocampal-dependent learning in mice. *Proc. Natl. Acad. Sci. USA* 101, 5111–5116. <https://doi.org/10.1073/pnas.0306336101>.
 87. Tiveron, M.-C., Beurrier, C., Céni, C., Andriambao, N., Combes, A., Koehl, M., Maurice, N., Gatti, E., Abrous, D.N., Kerkerian-Le Goff, L., et al. (2016). LAMP5 Fine-Tunes GABAergic Synaptic Transmission in Defined Circuits of the Mouse Brain. *PLoS One* 11, e0157052. <https://doi.org/10.1371/journal.pone.0157052>.
 88. Yu, B., Zhang, Q., Lin, L., Zhou, X., Ma, W., Wen, S., Li, C., Wang, W., Wu, Q., Wang, X., and Li, X.M. (2023). Molecular and cellular evolution of the amygdala across species analyzed by single-nucleus transcriptome profiling. *Cell Discov.* 9, 19. <https://doi.org/10.1038/s41421-022-00506-y>.
 89. Hodge, R.D., Bakken, T.E., Miller, J.A., Smith, K.A., Barkan, E.R., Graybuck, L.T., Close, J.L., Long, B., Johansen, N., Penn, O., et al. (2019). Conserved cell types with divergent features in human versus mouse cortex. *Nature* 573, 61–68. <https://doi.org/10.1038/s41586-019-1506-7>.
 90. Huang, T.-T., Zou, Y., and Corniola, R. (2012). Oxidative stress and adult neurogenesis—effects of radiation and superoxide dismutase deficiency. *Semin. Cell. Dev. Biol.* 23, 738–744. <https://doi.org/10.1016/j.semcd.2012.04.003>.
 91. Aguilera-Hernández, L., Alejandre, R., César Morales-Medina, J., Iannitti, T., and Flores, G. (2023). Cellular mechanisms in brain aging: Focus on physiological and pathological aging. *J. Chem. Neuroanat.* 128, 102210. <https://doi.org/10.1016/j.jchemneu.2022.102210>.
 92. Mattson, M.P., and Arumugam, T.V. (2018). Hallmarks of brain aging: adaptive and pathological modification by metabolic states. *Cell Metab.* 27, 1176–1199. <https://doi.org/10.1016/j.cmet.2018.05.011>.
 93. Dulken, B.W., Buckley, M.T., Navarro Negredo, P., Saligrama, N., Cayrol, R., Leeman, D.S., George, B.M., Boutet, S.C., Hebestreit, K., Pluvinage, J.V., et al. (2019). Single-cell analysis reveals T cell infiltration in old neurogenic niches. *Nature* 571, 205–210. <https://doi.org/10.1038/s41586-019-1362-5>.
 94. Radjavi, A., Smirnov, I., Derecki, N., and Kipnis, J. (2014). Dynamics of the meningeal CD4(+) T-cell repertoire are defined by the cervical lymph nodes and facilitate cognitive task performance in mice. *Mol. Psychiatr.* 19, 531–533. <https://doi.org/10.1038/mp.2013.79>.
 95. Ziv, Y., Ron, N., Butovsky, O., Landa, G., Sudai, E., Greenberg, N., Cohen, H., Kipnis, J., and Schwartz, M. (2006). Immune cells contribute to the maintenance of neurogenesis and spatial learning abilities in adulthood. *Nat. Neurosci.* 9, 268–275. <https://doi.org/10.1038/nn1629>.
 96. Bryan, K.J., Zhu, X., Harris, P.L., Perry, G., Castellani, R.J., Smith, M.A., and Casadesus, G. (2008). Expression of CD74 is increased in neurofibrillary tangles in Alzheimer's disease. *Mol. Neurodegener.* 3, 13. <https://doi.org/10.1186/1750-1326-3-13>.
 97. Matsuda, S., Matsuda, Y., and D'Adamio, L. (2009). CD74 interacts with APP and suppresses the production of Abeta. *Mol. Neurodegener.* 4, 41. <https://doi.org/10.1186/1750-1326-4-41>.
 98. Kiyota, T., Zhang, G., Morrison, C.M., Bosch, M.E., Weir, R.A., Lu, Y., Dong, W., and Gendelman, H.E. (2015). AAV2/1 CD74 Gene Transfer Reduces β-amyloidosis and Improves Learning and Memory in a Mouse Model of Alzheimer's Disease. *Mol. Ther.* 23, 1712–1721. <https://doi.org/10.1038/mt.2015.142>.
 99. Genon, S., Bernhardt, B.C., La Joie, R., Amunts, K., and Eickhoff, S.B. (2021). The many dimensions of human hippocampal organization and (dys)function. *Trends Neurosci.* 44, 977–989. <https://doi.org/10.1016/j.tins.2021.10.003>.
 100. Bienkowski, M.S., Sepehrband, F., Kurniawan, N.D., Stanis, J., Korobkova, L., Khanjani, N., Clark, K., Hintiryan, H., Miller, C.A., and Dong, H.-W. (2021). Homologous laminar organization of the mouse and human subiculum. *Sci. Rep.* 11, 3729. <https://doi.org/10.1038/s41598-021-81362-w>.
 101. Burwell, R.D. (2000). The parahippocampal region: corticocortical connectivity. *Ann. N. Y. Acad. Sci.* 911, 25–42. <https://doi.org/10.1111/j.1749-6632.2000.tb06717.x>.
 102. Witter, M.P., and Amaral, D.G. (2004). Hippocampal Formation. In *The Rat Nervous System*, G. Paxinos, ed. (Elsevier), pp. 635–704. <https://doi.org/10.1016/B978-012547638-6/50022-5>.
 103. Strange, B.A., Witter, M.P., Lein, E.S., and Moser, E.I. (2014). Functional organization of the hippocampal longitudinal axis. *Nat. Rev. Neurosci.* 15, 655–669. <https://doi.org/10.1038/nrn3785>.
 104. Miller, R., Page, S., and Ramnauth, A. (2023). LieberInstitute/spatial_DG_lifespan: v1.0.0 (Zenodo). <https://doi.org/10.5281/zenodo.10126688>.
 105. Ramnauth, A., Divecha, H., Collado-Torres, L., Tippani, M., and Miller, R. (2024). LieberInstitute/spatial_DG_lifespan: v1.0.2 (Zenodo). <https://doi.org/10.5281/zenodo.10126715>.
 106. Pardo, B., Spangler, A., Weber, L.M., Page, S.C., Hicks, S.C., Jaffe, A.E., Martinowich, K., Maynard, K.R., and Collado-Torres, L. (2022). spatialLIBD: an R/Bioconductor package to visualize spatially-resolved transcriptomics data. *BMC Genom.* 23, 434. <https://doi.org/10.1186/s12864-022-08601-w>.
 107. Tippani, M., Divecha, H.R., Catallini, J.L., Kwon, S.H., Weber, L.M., Spangler, A., Jaffe, A.E., Hyde, T.M., Kleinman, J.E., Hicks, S.C., et al. (2023). VistaSeg: Processing utilities for high-resolution images for spatially resolved transcriptomics data. *Biol. Imaging* 3, e23. <https://doi.org/10.1017/S2633903X23000235>.
 108. Lipska, B.K., Deep-Soboslay, A., Weickert, C.S., Hyde, T.M., Martin, C.E., Herman, M.M., and Kleinman, J.E. (2006). Critical factors in gene expression in postmortem human brain: Focus on studies in schizophrenia. *Biol. Psychiatry* 60, 650–658. <https://doi.org/10.1016/j.biopsych.2006.06.019>.
 109. 10x Genomics. Single-Library Analysis with spaceranger count. <https://support.10xgenomics.com/spatial-gene-expression/software/pipelines/latest/using/count>.
 110. Righelli, D., Weber, L.M., Crowell, H.L., Pardo, B., Collado-Torres, L., Ghazanfar, S., Lun, A.T.L., Hicks, S.C., and Risso, D. (2022). SpatialExperiment: infrastructure for spatially-resolved transcriptomics data in R using Bioconductor. *Bioinformatics* 38, 3128–3131. <https://doi.org/10.1093/bioinformatics/btac299>.
 111. Maynard, K.R., Collado-Torres, L., Weber, L.M., Uytingco, C., Barry, B.K., Williams, S.R., Catallini, J.L., Tran, M.N., Besich, Z., Tippani, M., et al. (2021). Transcriptome-scale spatial gene expression in the human dorsolateral prefrontal cortex. *Nat. Neurosci.* 24, 425–436. <https://doi.org/10.1038/s41593-020-00787-0>.
 112. Weber, L.M., Divecha, H.R., Tran, M.N., Kwon, S.H., Spangler, A., Montgomery, K.D., Tippani, M., Bharadwaj, R., Kleinman, J.E., Page, S.C., et al. (2024). The gene expression landscape of the human locus coeruleus revealed by single-nucleus and spatially-resolved transcriptomics. *Elife* 12, RP84628. <https://doi.org/10.7554/eLife.84628>.
 113. McCarthy, D.J., Campbell, K.R., Lun, A.T.L., and Wills, Q.F. (2017). Scater: pre-processing, quality control, normalization and visualization of single-cell RNA-seq data in R. *Bioinformatics* 33, 1179–1186. <https://doi.org/10.1093/bioinformatics/btw777>.

114. Lun, A.T.L., McCarthy, D.J., and Marioni, J.C. (2016). A step-by-step workflow for low-level analysis of single-cell RNA-seq data with Bioconductor. [version 2; peer review: 3 approved, 2 approved with reservations]. F1000Res. 5, 2122. <https://doi.org/10.12688/f1000research.9501.2>.
115. Korsunsky, I., Millard, N., Fan, J., Slowikowski, K., Zhang, F., Wei, K., Ba-glaenko, Y., Brenner, M., Loh, P.-R., and Raychaudhuri, S. (2019). Fast, sensitive and accurate integration of single-cell data with Harmony. *Nat. Methods* 16, 1289–1296. <https://doi.org/10.1038/s41592-019-0619-0>.
116. Amezquita, R.A., Lun, A.T.L., Becht, E., Carey, V.J., Carpp, L.N., Geistlinger, L., Marini, F., Rue-Albrecht, K., Risso, D., Soneson, C., et al. (2020). Orchestrating single-cell analysis with Bioconductor. *Nat. Methods* 17, 137–145. <https://doi.org/10.1038/s41592-019-0654-x>.
117. Scrucca, L., Fop, M., Murphy, T.B., and Raftery, A.E. (2016). mclust 5: Clustering, Classification and Density Estimation Using Gaussian Finite Mixture Models. *Rom. Jahrb.* 8, 289–317. <https://doi.org/10.32614/RJ-2016-021>.
118. Lun, A. (2022). bluster: Clustering Algorithms for Bioconductor. R package version 1.8.0. Bioconductor 1. <https://doi.org/10.18129/b9.bioc.bluster>.
119. Robinson, M.D., McCarthy, D.J., and Smyth, G.K. (2010). edgeR: a Bioconductor package for differential expression analysis of digital gene expression data. *Bioinformatics* 26, 139–140. <https://doi.org/10.1093/bioinformatics/btp616>.
120. Boyle, E.I., Weng, S., Gollub, J., Jin, H., Botstein, D., Cherry, J.M., and Sherlock, G. (2004). GO::TermFinder—open source software for accessing Gene Ontology information and finding significantly enriched Gene Ontology terms associated with a list of genes. *Bioinformatics* 20, 3710–3715. <https://doi.org/10.1093/bioinformatics/bth456>.
121. Wu, T., Hu, E., Xu, S., Chen, M., Guo, P., Dai, Z., Feng, T., Zhou, L., Tang, W., Zhan, L., et al. (2021). clusterProfiler 4.0: A universal enrichment tool for interpreting omics data. *Innovation* 2, 100141. <https://doi.org/10.1016/j.xinn.2021.100141>.
122. DeBruine, Z.J., Melcher, K., and Triche, T.J. (2021). Fast and robust non-negative matrix factorization for single-cell experiments. bioRxiv. <https://doi.org/10.1101/2021.09.01.458620>.
123. Li, H., Zhou, J., Li, Z., Chen, S., Liao, X., Zhang, B., Zhang, R., Wang, Y., Sun, S., and Gao, X. (2023). A comprehensive benchmarking with practical guidelines for cellular deconvolution of spatial transcriptomics. *Nat. Commun.* 14, 1548. <https://doi.org/10.1038/s41467-023-37168-7>.
124. Marioni, R.E., Shah, S., McRae, A.F., Chen, B.H., Colicino, E., Harris, S.E., Gibson, J., Henders, A.K., Redmond, P., Cox, S.R., et al. (2015). DNA methylation age of blood predicts all-cause mortality in later life. *Genome Biol.* 16, 25. <https://doi.org/10.1186/s13059-015-0584-6>.
125. Dutta, S., and Sengupta, P. (2016). Men and mice: Relating their ages. *Life Sci.* 152, 244–248. <https://doi.org/10.1016/j.lfs.2015.10.025>.
126. Wang, S., Lai, X., Deng, Y., and Song, Y. (2020). Correlation between mouse age and human age in anti-tumor research: Significance and method establishment. *Life Sci.* 242, 117242. <https://doi.org/10.1016/j.lfs.2019.117242>.
127. Nishiyama, A., Shimizu, T., Sherafat, A., and Richardson, W.D. (2021). Life-long oligodendrocyte development and plasticity. *Semin. Cell Dev. Biol.* 116, 25–37. <https://doi.org/10.1016/j.semcdb.2021.02.004>.
128. Wickham, H. (2016). ggplot2 - Elegant Graphics for Data Analysis, 2nd ed. (Springer International Publishing). <https://doi.org/10.1007/978-3-319-24277-4>.
129. Chang, W., Cheng, J., Allaire, J.J., Xie, Y., and McPherson, J. (2019). Shiny: Web Application Framework for R (Packt Publishing Ltd).

STAR★METHODS

KEY RESOURCES TABLE

REAGENT or RESOURCE	SOURCE	IDENTIFIER
Biological Samples		
Human postmortem brain hippocampal tissue	Lieber Institute for Brain Development; see Table S1	N/A
Chemicals, Peptides, and Recombinant Proteins		
O.C.T. Compound	Tissue-Tek Sakura	product code 4583
10% neutral buffered formalin	Sigma-Aldrich	catalog no. HT501128
Opal Fluorophore 520	Akoya Biosciences	catalog no. FP1487001KT
Opal Fluorophore 570	Akoya Biosciences	catalog no. FP1488001KT
Opal Fluorophore 620	Akoya Biosciences	catalog no. FP1495001KT
Opal Fluorophore 690	Akoya Biosciences	catalog no. FP1497001KT
Fluoromount-G	ThermoFisher	catalog no. 00-4958-02
Critical Commercial Assays		
Visium Tissue Optimization Slides	10x Genomics	catalog no. 3000394
Visium Spatial Gene Expression Slides	10x Genomics	catalog no. 2000233
RNAscope Multiplex Fluorescent Kit, v2	Advanced Cell Diagnostics	catalog no. 323100
RNAscope 4-Plex Ancillary Kit	Advanced Cell Diagnostics	catalog no. 323120
RNAscope Probe- Hs-PROX1	Advanced Cell Diagnostics	catalog no. 530241
RNAscope Probe- Hs-LAMP5	Advanced Cell Diagnostics	catalog no. 487691-C2
RNAscope Probe- Hs-GAD1	Advanced Cell Diagnostics	catalog no. 404031-C3
RNAscope Probe- Hs-SLC17A7	Advanced Cell Diagnostics	catalog no. 415611-C4
Deposited Data		
Raw sequencing read data	This paper	SRA Accession number: PRJNA1043093
Two <i>SpatialExperiment</i> objects (one untransformed and another batch-corrected with log-normalization)	This paper	https://doi.org/10.5281/zenodo.10126687
Software and Algorithms		
Loupe browser v.6.0.0	10x Genomics	https://www.10xgenomics.com/support/software/loupe-browser/latest/release-notes/lb-release-notes#6-0-0-247894
SpaceRanger v.1.3.1	10x Genomics	https://www.10xgenomics.com/support/software/space-ranger/latest/release-notes/release-notes-for-SR#space-ranger-v-1-3-1-november-1-2021-b5ba13
NIS-Elements v.5.42.02	Nikon	https://www.microscope.healthcare.nikon.com/products/software/nis-elements
VistoSeg	Tippanni et al. ¹⁰⁷	https://doi.org/10.1017/S2633903X23000235
R Programming Language v.4.2.1	R Core Team	https://www.r-project.org/
Bioconductor v.3.15.2	R package	https://www.bioconductor.org/
SpatialExperiment v.1.6.1	R package	https://bioconductor.org/packages/release/bioc/html/SpatialExperiment.html
scuttle v.1.6.2	R package	https://bioconductor.org/packages/release/bioc/html/scuttle.html
scran v.1.24.0	R package	https://bioconductor.org/packages/release/bioc/html/scran.html
scater v.1.24.0	R package	https://bioconductor.org/packages/release/bioc/html/scater.html

(Continued on next page)

Continued

REAGENT or RESOURCE	SOURCE	IDENTIFIER
harmony v.0.1.0	R package	https://portals.broadinstitute.org/harmony/
SingleCellExperiment v.1.18.0	R package	https://bioconductor.org/packages/release/bioc/html/SingleCellExperiment.html
spatialLIBD v.1.12.0	R package	https://bioconductor.org/packages/release/data/experiment/html/spatialLIBD.html
shiny v.1.7.5	R package	https://shiny.posit.co/r/reference/shiny/
BayesSpace v.1.6.0	R package	https://bioconductor.org/packages/release/bioc/html/BayesSpace.html
bluster v.1.10.0	R package	https://bioconductor.org/packages/release/bioc/html/bluster.html
edgeR v.3.38.4	R package	https://bioconductor.org/packages/release/bioc/html/edgeR.html
clusterProfiler v.4.4.4	R package	https://bioconductor.org/packages/release/bioc/html/clusterProfiler.html
RcppML v.0.5.5	R package	https://zdebruine.github.io/RcppML/
reticulate v.1.28	R package	https://rstudio.github.io/reticulate/
CoGAPS v3.20.0	R package	https://bioconductor.org/packages/release/bioc/html/CoGAPS.html
VISION v.3.0.1	R package	https://yoseflab.github.io/VISION/
Other		
Code for analyses in the present study	This paper	https://doi.org/10.5281/zenodo.10126715 and https://github.com/LieberInstitute/spatial_DG_lifespan
Interactive web-based app	This paper	https://libd.shinyapps.io/Lifespan_DG/

EXPERIMENTAL MODEL AND STUDY PARTICIPANT DETAILS

Postmortem human brain tissue from male and female neurotypical donors ($n = 17$) of European and/or African ancestry spanning ages 0.18 to 76.7 years were obtained by brain donations collected through the following locations and protocols at the time of autopsy: the Office of the Chief Medical Examiner of the State of Maryland, under the Maryland Department of Health's IRB protocol #12–24, the Departments of Pathology at Western Michigan University Homer Stryker MD School of Medicine and the University of North Dakota School of Medicine and Health Sciences, and the County of Santa Clara Medical Examiner-Coroner Office, all under WCG IRB protocol #20111080. One additional sample was consented through the National Institute of Mental Health Intramural Research Program (NIH protocol #90-M-0142), and was acquired by LIBD via material transfer agreement. All donors were obtained with informed consent from the legal next of kin. Demographics (including biological sex and race as reported by next-of-kin) and cause of death for the 17 donors are listed in Table S1. Audiotaped and witnessed informed consent was obtained from the legal next-of-kin for every case. The LIBD Autopsy telephone screening was done at time of donation with the legal next-of-kin, and consisted of 39 items about the donor's medical, social, psychiatric, substance use, and treatment history. Retrospective clinical diagnostic reviews were conducted for every brain donor to include data from: autopsy reports, toxicology testing, forensic investigations, neuropathological examinations, telephone screening, and psychiatric/substance abuse treatment record reviews and/or supplemental family informant interviews. All data was compiled and summarized in a detailed psychiatric narrative summary, and was reviewed independently by two board-certified psychiatrists in order to determine lifetime psychiatric and substance use disorder diagnoses according to Diagnostic and Statistical Manual of Mental Disorders, Fifth Edition (DSM-5). All donors in this study had no lifetime history of a psychiatric or substance use disorder according to DSM-5. All donors were negative for illicit drugs of abuse at time of death. Donors were further excluded if they had evidence of neuropathological abnormalities including cerebrovascular accidents, neuritic pathology, or other brain abnormalities. Details of tissue acquisition, handling, processing, dissection, clinical characterizations, diagnoses, neuropathological examinations, RNA extraction and quality control (QC) measures have been described previously.¹⁰⁸ Samples were allocated to experimental age groups based on age at time of death: infant (0–2 years), teen (13–18 years), adult (30–50 years), and elderly (70+ years). The anterior half of the HPC containing dentate gyrus was microdissected using a hand-held dental drill as previously described,⁵⁷ staying within the anterior half of the HPC as guided by visual inspection of the HPC itself, anterior to the appearance of the lateral geniculate nucleus and progressive diminution of the putamen. Tissue blocks were then stored at -80°C .

METHOD DETAILS**Tissue processing and quality control**

Frozen brain blocks were embedded on the posterior end in OCT (TissueTek Sakura) and cryosectioned at -10°C (Thermo Cryostar). Brain blocks were cryosectioned and stained with hematoxylin and eosin (H&E) to verify the presence of anatomical landmarks of the dentate gyrus such as the GCL. Sections were placed on chilled Visium Tissue Optimization Slides (catalog no. 3000394, 10x Genomics) and Visium Spatial Gene Expression Slides (catalog no. 2000233, 10x Genomics), and adhesion of tissue to slide was facilitated by warming the back of the slide. Tissue sections were then fixed in chilled methanol, and stained according to the Methanol Fixation, H&E Staining & Imaging for Visium Spatial Protocol (catalog no. CG000160 Rev C, 10x Genomics) or Visium Spatial Tissue Optimization User Guide (catalog no. CG000238 Rev C, 10x Genomics). Visium Tissue Optimization Slides were used to choose the optimal permeabilization time. For gene expression experiments, tissue was permeabilized for 18 min, which was selected as the optimal time based on tissue optimization time-course experiments. Brightfield histology images of H&E stained sections were taken on a Leica Aperio CS2 slide scanner equipped with a color camera and a 20x/0.75 NA objective with a 2x optical magnification changer for 40x scanning, or on an Olympus VS200 slide scanner equipped with a 10x/0.4NA objective. For tissue optimization experiments, fluorescent images were taken with a Cyvation C10 Confocal Imaging Reader (Agilent) equipped with TRITC filter (ex 556/em 600 \times) and 10 \times objective at approximately 400ms exposure time. Sample Br3874 contained no GCL as verified by H&E staining and incorrect spatial domain assignment by BayesSpace and was removed from downstream analyses ([Figure S3](#)).

Visium data generation

Libraries were prepared according to the Visium Spatial Gene Expression User Guide (CG000239 Rev C, 10x Genomics). For two slides, Visium Spatial Gene Expression Slides were shipped to 10x Genomics after tissue mounting for H&E staining, imaging, cDNA synthesis, and library preparation. Libraries were quality controlled with Agilent Bioanalyzer High Sensitivity dsDNA chips and sequenced on a NovaSeq 6000 System (Illumina) at a sequencing depth of a minimum of 60,000 reads per Visium spot. Sequencing was performed using the following read protocol: read 1: 28 cycles; i7 index read: 10 cycles; i5 index read: 10 cycles; and read 2: 90 cycles.

Single-molecule fluorescent *in situ* hybridization (smFISH) and imaging

Infant ($n = 2$) and adult ($n = 3$) hippocampal sections (10 μm) were fixed in 10% neutral buffered formalin (catalog no. HT501128, Sigma-Aldrich) for 30 min at RT, followed by ethanol-based serial dehydration. Hybridization assays were performed according to manufacturer instructions using the RNAscope Multiplex Fluorescent Reagent Kit V2 (catalog no. 323100, Advanced Cell Diagnostics [ACD]) and the 4-plex ancillary kit V2 (catalog no. 323120, ACD). Briefly, sections were pretreated with hydrogen peroxide for 10 min and then permeabilized with Protease IV for 30 min at RT. Probes for *PROX1* (catalog no. 530241, ACD), *LAMP5* (catalog no. 487691-C2, ACD), *GAD1* (catalog no. 404031-C3, ACD), and *SLC17A7* (catalog no. 415611-C4, ACD) were applied to the slide and allowed to hybridize for 2 h at 40°C . Slides were washed briefly and stored in 4x saline sodium citrate (catalog no. 351-003-101, Quality Biological) overnight at 4°C . The next day, probes were amplified and fluorescently labeled with Opal dyes as follows: *PROX1* was labeled with 1:500 Opal 520 (catalog no. FP1487001KT, Akoya Biosciences [AB]), *LAMP5* was labeled with 1:500 Opal 690 (catalog no. FP1497001KT, AB), *GAD1* was labeled with 1:500 Opal 570 (catalog no. FP1488001KT, AB) and *SLC17A7* was labeled with 1:500 Opal 620 (catalog no. FP1495001KT, AB). DAPI was applied to each slide for 20 s prior to mounting with Fluoromount-G (catalog no. 00-4958-02, ThermoFisher).

Slides were imaged on an AX Nikon Ti2-E confocal fluorescence microscope equipped with NIS-Elements (v5.42.02). The DG, from the ML to the CA4, was captured with a combination of tiles (30–60 tiles/image, 2048 x 2048 pixels per tile) and z-stacks (7 steps, 2 μm /step, 12 μm range) at 20x magnification (Nikon PLAN APO λ 20x/0.80) with a pinhole of 1.0 AU. Fluorescently-tagged probes were captured using a custom 6-channel, 3-track experiment setup that includes DAPI (405nm excitation laser, 420-500nm filter), Opal 520 (488nm excitation laser, 500-535nm filter), Opal 570 (561nm excitation laser, 580-600nm filter), Opal 620 (561nm excitation laser, 610-630nm filter), Opal 690 (640nm excitation laser, 675-700nm filter) and a lipofuscin channel (488nm excitation laser, 700-750nm filter). All images were captured using the same laser power (LP) and gain (G) settings as follows: DAPI: 28 LP/5 G, Opal 520: 28 LP/5 G, Opal 570: 6 LP/2 G, Opal 620: 6 LP/0.5 G, Opal 690: 9 LP/1 G, Lipo: 28 LP/15 G. After capture, individual tiles were stitched together prior to max-intensity projecting. Linear unmixing was performed using Opal dye spectral standards and a human postmortem lipofuscin spectral standard. Opal dye standards were previously created using single-positive *Polr2a* stained, wild-type mouse, coronal sections, where each section was stained singularly with one Opal dye (520, 570, 620, 690). After images were unmixed, they were exported as single channel.tiff files.

QUANTIFICATION AND STATISTICAL ANALYSIS**Visium raw data processing**

The manual alignment of raw histology images were processed by sample using 10x Genomics Loupe browser [v.6.0.0]. Raw sequencing data files (FASTQ files) for the sequenced libraries were processed using 10x Genomics SpaceRanger software [v. 1.3.1], which uses human genome reference transcriptome version GRCh38 2020-A (July 7, 2020) provided by 10x Genomics

for genome alignment.¹⁰⁹ The preprocessed Visium data for each sample, integrated with the output from VistoSeg¹⁰⁷ (see Methods Section 4.5, Visium-H&E image segmentation and processing), were stored in an R/Bioconductor S4 class using the SpatialExperiment v.1.6.1 R/Bioconductor package.¹¹⁰

Visium-H&E image segmentation and processing

Nuclei segmentation was performed using VistoSeg, a MATLAB-based software package¹⁰⁷ for samples for which sufficiently high resolution images were acquired (Figure S15). Briefly, Gaussian smoothing and contrast adjustment were performed to enhance the nuclei in the image. The image is converted L*a*b color space. The a*b color space is extracted from the L*a*b-converted image and is given to a K-means clustering function, along with the number of colors (k) the user visually identifies in the image; here $k = 5$. The function outputs a binary mask for each of the (k) distinguishable color gradients in the image. The segmentation is further refined by extracting the intensity of the pixels from the binary mask of nuclei and applying an intensity threshold to separate the darker nuclei regions at center from the lighter regions at the borders. Loupe Browser v.6.0.0 produces a JSON file for each full-resolution capture area tiff from VistoSeg, encoding properties of the image e.g., spot diameter in pixels. SpaceRanger provides a.csv file for each full-resolution capture area tiff that includes information for each spot with an identification barcode and pixel coordinates for the center of the spots. The VistoSeg package integrates these files with the segmented imaging data to provide a final table with nuclei count per Visium spot for each capture area.

Spot-level data processing

All Visium data analyses were performed using a SpatialExperiment (spe) S4 class storing the object constructed with the SpatialExperiment v.1.6.1 R/Bioconductor package.¹¹⁰ The spe class extends the SingleCellExperiment class used for scRNA-seq data for spatial context, with observations at the level of Visium spots rather than cells. Objects in the spe class hold additional spatial information e.g., colData has information on whether Visium spots overlap with the tissue from imaging data, spatialCoords has the x- and y-coordinates of the Visium capture areas, and imgData holds the imaging files and information pertaining to the images (such as pixel resolution). To the spe class, we added information including the sum of segmented cells per spot computed from the VistoSeg package, the sum of UMIs per spot, the sum of genes expressed per spot, donor age, donor sex, RNA integrity numbers (RIN), race, and postmortem interval (PMI) in hours.

Spot level analysis was performed as previously described.^{56,111,112} Briefly, spot level quality control (QC) were evaluated using the perCellQCMetrics() function from the scuttle package v.1.6.2 R Bioconductor package¹¹³ and low quality spots having low UMI counts, low gene counts, or high percent of mitochondrial genetic expression were dropped using the isOutlier() function of the same package (Figures S1 and S2). The scran v.1.24.0 R Bioconductor package¹¹⁴ functions quickCluster() (blocking for each brain donor) and computeSumFactors(), then logNormCounts() function from the scuttle package were used to compute the log-transformed and normalized gene expression counts at the spot level. The scran package function modelGeneVar() was used to model the gene mean expression and variance (blocking for each brain donor), and getTopHVGs() was used to identify the top 10% HVGs. The top 10% HVGs were used to compute 50 principal components (PCs) with the runPCA() function from scater v.1.24.0 R Bioconductor package and runUMAP(), from the same package, was used for Uniform Manifold Approximation and Projection (UMAP) dimensionality reduction.¹¹³ Primarily for the purposes of unsupervised spatial clustering, corrections for potential batch effects and high dataset variabilities were performed by employing an transcriptomic data integration algorithm that projects Visium spots into a shared dimensionally reduced PC embedding (Harmony embeddings), which encourages spots to group by spot type rather than by dataset-specific conditions (Figure S4). The above mentioned algorithm was implemented by employing the HarmonyMatrix() function from the Harmony v.0.1.0 R package¹¹⁵ on a matrix containing reduced dimension coordinates for Visium spots in PC space constructed with the reducedDim() function from the SingleCellExperiment v.1.18.0 R Bioconductor package.¹¹⁶ This results in a QCed and batch-corrected spe object.

Spatial domain detection and annotation

To enable inspection of the spe, we generated an interactive shiny v.1.7.5 R package web application at https://lbd.shinyapps.io/Lifespan_DG/ using spatialLIBD v.1.12.0 R Bioconductor package.¹⁰⁶ A blinded experimenter (A.R.P.) manually assigned spots to anatomical domains following consideration of marker gene expression and histological staining (Figure S7). Simultaneously, generation of unsupervised spatial domains were performed on the spe object by a separate experimenter (A.D.R.) using the spatialCluster() function from the BayesSpace v.1.6.0 R Bioconductor package⁵⁵ as previously described⁵⁶ (Figures 1C and S5). Briefly, the number of clusters are determined *a priori* by biological/anatomical knowledge and fixed prior to spatial clustering. For each Visium spot, a low dimensional representation of the gene expression vector is obtained from the Harmony embeddings. Bayesian priors are determined by an initial non-spatial clustering with Mclust¹¹⁷ and compared with a Markov random field given by the Potts model, which encodes information on all the spots and their neighboring spots; this allows for smoothing of initial clusters by encouraging neighboring spots to be grouped in the same cluster. The resulting Bayesian model is a fixed precision matrix model, where iterative Gibbs sampling is used for updating most of the parameters in the Metropolis–Hastings algorithm; Markov chain Monte Carlo (MCMC) method is used to update latent clusters iteratively produced by the Potts model. The mode (average) of the chain for each cluster label of a spot is assigned as the final cluster label of that spot. The number of repetitions was set empirically via trial by trial basis. We chose $k = 10$ as the number of clusters and ran BayesSpace at 50,000 iterations. At $k > 10$ we saw less smoothing

of spatial domains and bifurcation of the GCL into two clusters with mixing of the ML. Domain 7 is enriched for GCL markers *PROX1* and *CALB1*. Domain 6 is enriched for interneuron markers characteristic of the subgranular zone (SGZ) including *GAD1*, *GAD2*, and *SST*. Domain 4 expresses markers of both CA3 and CA4 including *KIT* and *TRHDE*, and was thus classified as ‘CA3&4’ (Figures 1C and S6). Domain 2 is enriched for synaptic markers including *CAMK2A* and the mitochondrial gene *MT-ND6*, characteristic of the neuropil-rich ML (Figures S5 and S6). Remaining domains were annotated based on anatomical location and expression of canonical marker genes (Figures 1C, S5, and S6). Additionally, we noted that some of the capture areas contained thalamic regions, which are enriched for inhibitory cell markers and partially included in spatial domain 6 (Figures S5 and S6). Since this could interfere with differential expression results pertaining to the SGZ, we set a threshold of logcount <1 for expression of the pan-thalamic marker *TCF7L2*, which removed virtually all thalamus-containing Visium spots (Figure S5B). A total of 65,782 spots were included in pseudobulk and differential expression analysis. To assess cluster neighborhood purity for each Visium spot, we used the neighborPurity() function from the bluster v.1.10.0 Bioconductor package, which uses a hypersphere-based approach to compute the “purity” of each cluster based on the number of contaminating spots from different clusters in its neighborhood (Figure S8).

Spatial domain comparison

Comparison of predicted spatial domains to manual annotations using principal components (PCA) and Uniform Manifold Approximation and Projection (UMAP)¹¹³ visualization revealed less intermingling of spot cluster labels in expression space for predicted domains, suggesting overclustering and/or mixing of cluster labels at spatial domain borders by manual annotation (Figures S8A–S8C and Table S2). We also evaluated predicted spatial domain quality using cluster purity¹¹⁸, and found higher purity in predicted spatial domains compared to manual annotations (Figure S8D).

Spatial domain-level processing

For gene modeling and functional enrichment analyses, the spots were pseudo-bulked by the generated spatial domain and donor, as previously described.^{56,111} Briefly, taking the QCed and batch-corrected *spe* object, we summed the raw gene-expression counts, for a given gene, across all spots in a given donor and a given spatial domain, and repeated this procedure for each gene with the aggregateAcrossCells() function from the scuttle package. We filtered for genes that have statistically sufficiently large counts in the pseudo-bulked spatial domains with the filterByExpr() function and calculated log normalized counts with the calcNormFactors() function, both functions from the edgeR v.3.38.4 R Bioconductor package.¹¹⁹ We also filtered for pseudo-bulked low Visium spot count by setting a threshold for >50 spots. Principal component analysis of the pseudo-bulked spots revealed that BayesSpace domain 3 had variation in many of the principal components that separated it from the other clusters, thus minimizing the variance between HPC spatial domains (Figure S9). Examination of cluster 3 gene markers suggested that this cluster was choroid plexus (CP) (Figures 1C and S6), a cerebrospinal fluid-producing secretory tissue. To prevent masking of variance within the HPC proper, BayesSpace domain 3 was removed from downstream analyses.

To reduce sparsity and increase UMI coverage of genes, we combined the ML, GCL, SGZ, and CA3&4 spatial domains *in silico* to generate a composite DG for age-associated comparisons (Methods, Figures 2A and S5, and S10). We performed differential expression (DE) analysis on the pseudo-bulked data to compare the composite DG in each age group to all other age groups (Table S3). We included CA3&4 in the composite DG because, in humans, this region contains mossy cells and interneurons as well as CA3 pyramidal neurons.¹⁵ Some tissue sections contained other HPC spatial domains, but they were not equally represented across donors (Figures S5 and S10) and were not included in composite DG analyses.

Spatial domain-level gene modeling of age groups

Using the pseudo-bulked spatial domain-level data, spatial domains of interest were isolated or combined and the pseudoBulkDGE() function, from the edgeR v.3.38.4 R Bioconductor package, was used following the limma-voom method with eBayes for differential modeling comparing one age group to all of the other age groups. We computed Student’s t-test statistics, $\log_2 FC$, and adjusted p -values.

For comparing differential expression across the pseudo-bulked spatial domain-level data, gene modeling was performed using the spatialLIBD package. Briefly, the BayesSpace spatial domain labels were set as the registration_variable. The registration_model() function was used to define the statistical model for computing the block correlation, with age and sex as covariates. The registration_block_cor() function was used to compute the block correlation using the donor sample IDs as the blocking factor. Then the functions registration_stats_enrichment(), registration_stats_pairwise(), registration_stats_anova() were used, employing the limma-voom method with eBayes, to fit enrichment, pairwise, and ANOVA models, respectively.

Functional enrichment analyses

Lists of genes with adjusted p -values <0.05 were compiled from pseudo-bulked spatial domains and age groups after DE analysis with pseudoBulkDGE() (Tables S3 and S5). Each list of genes were computed with Over Representation Analysis (ORA)¹²⁰ to determine whether known biological functions are over-represented in each spatial domain or age group, by large gene expression differences, for the following aspects: cellular component (intracellular locations where gene products are active, CC), molecular function (documented molecular activities associated with gene products, MF), and biological processes (sets of pathways and broader biological functions made up of the activities of multiple gene products, BP, Table S4). ORA was computed with the

enrichGO() function as an argument within the compareCluster() function from the clusterProfiler v.4.4.4 R Bioconductor package.¹²¹

We compiled a list of differentially expressed genes for superfine cell class GC.3 versus all other superfine cell classes, and GC.4 versus all other superfine cell classes, using the pseudobulked DE results taken from Thompson*, Nelson*, Tippani* et al., 2024⁶² with FDR <0.05, along with their logFC values (Figure S21). Each list of ordered genes with their logFC were further subdivided into lists with positive logFC and lists with negative logFC, to represent upregulation and downregulation. They were then computed with gene set enrichment analysis (GSEA) for all ontology categories (CC, MF, and BP). GSEA was computed with the gseGO() function as an argument within the compareCluster() function from the clusterProfiler v.4.4.4 R Bioconductor package.

Transfer learning of NMF patterns

Non-negative matrix factorization (NMF) is a dimensionality reduction technique where the resulting latent factors can identify patterns of coordinated gene expression that correlate with biological processes, including cell type and cell state.⁶¹ NMF as generally applied to gene expression data takes as input a normalized \log_2 counts matrix (genes x observations). This is factored into two lower-rank, orthogonal matrices: one with dimensions genes x k (h) and one with dimensions k x observations (w). Here, k represents NMF rank, which corresponds with the number of patterns specified by the user. The h and w matrices correspond with the observation-level and gene-level loadings, respectively, for k NMF patterns. NMF patterns generated from one dataset can predict the presence and distribution of these same latent factors in another dataset via transfer learning.⁶¹ We recently used this strategy to identify 100 NMF patterns from adult human HPC snRNA-seq data, which was integrated with paired Visium data from adjacent HPC tissue sections.⁶² For predicting NMF patterns in other scRNA-seq, snRNA-seq, and SRT datasets, we used the project() function, which takes the gene-level loadings in h , for the shared genes between datasets, as input to impute/predict the w (k x observations) matrix and thus the cell-level, nuclei-level, or Visium spot-level loadings for all the NMF patterns. We used the RcppML v.0.5.5 R package¹²² for NMF-based transfer learning as previously described.⁶² Following pattern transfer, NMF pattern weights were normalized to sum to 1 for each transcriptomic dataset.

Spot-level deconvolution of cell types

To perform spot-level deconvolution of cell types within each gene expression spot, we used publicly available snRNA-seq data.³⁹ To complement the design of this study, which targeted the DG, we truncated the Franjic et al., 2022 data to only the DG ($n = 102,753$ nuclei) for use as a reference dataset (Figure S23)³⁹ and using cell2location v0.1.3 Python package,^{67,123} as previously described.¹¹² Briefly, negative binomial regression was performed to estimate reference cell type signatures. Cell2location establishes Bayesian priors of cell abundances by using the Visium spatial and count data, and two manually entered hyperparameters: N_cells_per_location = 5 and detection_alpha = 20. A value of 3 for N_cells_per_location is typically recommended for cortex, but, due to the cell density within the GCL, we increased the estimation (Figure S15). To ensure unique gene expression profiles for optimized performance, we collapsed cell subtype clusters for granule cells (GC), CA1, somatostatin inhibitory neurons (InN_SST), parvalbumin inhibitory neurons (InNPV), vasointestinal peptide inhibitory neurons (InN_VIP), NR2F2 inhibitory neurons (InN_NR2F2), LAMP5 inhibitory neurons (InN_LAMP5), oligodendrocyte precursors, oligodendrocytes (Oligo), microglia, endothelial cells (Endo), and smooth muscle cells (SMC). Variational Bayesian Inference is employed to produce posterior distributions of estimated cell abundances (Figures S24 and S25). The mean of these distributions were then assigned to each spot. Cell proportions per spot were derived from the mean cell abundances per spot. To assess cell type heterogeneity of Visium spots, PCA was used to extract the top components of variation for cell type proportions for all spots (Figure S30), as previously done to assess cell type heterogeneity in blood.¹²⁴

Aging gene signature generation and score calculation

Computation of the common aging score (CAS) was performed similarly as previously described.⁶⁸ Using each individual pseudobulked spatial domain-level data to control for differences in spatial domains, the pseudoBulkDGE() function, from the edgeR v.3.38.4 R Bioconductor package, was used following the limma-voom method with eBayes for differential modeling comparing each age group (teen, adult, elderly) to the infant age group within each of the 9 pseudo-bulked spatial domains (DG: ML, GCL, SGZ, CA3&4, nonDG: CA1, SLM, SL, SR, WM, excluding CP). We computed Student's t-test statistics, \log_2 FC, and adjusted p-values. Membership in the aging signature gene set was determined by being a DEG in at least two of the age-associated differential modeling with thresholds of adjusted p-values smaller than 0.05 and a \log_2 fold change of at least 1.5, and shared by at least 3 spatial domains. The constructed signed gene set assigned genes with a value of 1 if positively associated with aging and -1 if negatively associated with aging. This produced a minimal, signed (+/-), gene set of 46 (+) and 13 (-) genes associated with human aging relative to the infant group (Table S6). The Visium QCed count data, with no log normalization, was UMI-scaled and, along with the signed gene set, used as input for the Visium function then further processed with the analyze function from the VISION package v.3.0.1. Briefly, signature aging scores for every spot is calculated with the analyze function by first log-transformation and removing global cell-specific distributional effects from the signature scores by Z-normalizing the expression data, then taking the sum of expression values for positive genes minus the sum of expression values for the negative genes divided by the total amount of genes in the signed gene set. This results in a score that summarizes the contrast between the positive and negative signed gene set (Table S6 and Figure S28).

To construct CAS velocities, linear modeling of CAS from age and spatial domain was performed with the lm() function in R. The lstromds() function from the lsmeans package v.2.30.0 with Tukey's HSD test within all possible spatial domain-to-spatial domain comparisons was used to estimate and compare the slopes of fitted lines for each spatial domain to assess significant slope differences. In the mouse CAS study,⁶⁸ the youngest age group was 3 months old, which approximately correlates to humans in their mid-twenties.^{125,126} As a result, although we do see similarities in spatial assignment of mouse-derived CAS values (Figure S31A), our human-derived values were more sensitive to spots enriched for oligodendrocytes (Figures 6C and 6D, S29, S30, and S31B). Comparing our human DG CAS values to those derived from the whole mouse brain⁶⁸ highlights the importance of including younger ages in developmental comparisons of age-associated gene expression changes.

To assess if CAS was solely driven by cell type changes over lifespan, we investigated the relationship between CAS and cell type proportions in each spot. Using the outputs from cell2location (Figures S24 and S25), we applied PCA to extract the top components of variation for highest predicted cell type proportion per spot.¹²⁴ Differences in the predicted cell type proportions were not sufficient to explain the majority of variation in CAS values (Figure S30), although PCs 1–4 explain 38% of the variation between spot-level CAS values and highest predicted cell type proportion per spot. We note that the relationship was particularly strong for oligodendrocytes, but we do not detect major differences in the proportion of spots from WM with age (Figure S10), and thus this relationship may be driven by increased oligodendrogenesis post-infancy¹²⁷ rather than differences in WM amount per sample.

Reproducibility

No statistical methods were used to predetermine sample sizes. Table S1 contains the demographic information for the 17 donors in the study. All boxplots display the median as the center, interquartile ranges (IQR) (25th & 75th percentiles) as the box edges, and 1.5× the IQR for the whiskers. All reported p values were two sized and were adjusted for multiple testing with Benjamini-Hochberg correction unless otherwise stated. Distributions of the residuals of the linear modeling were assumed to be normally distributed across all genes and models, but this was not formally tested. Wilcoxon signed-rank test used for comparing mean cell abundances between two age groups. Tukey's HSD test was used across all possible spatial domain-to-spatial domain comparisons of CAS slopes. Spots that were outside of tissue or did not pass QC checks were omitted from all analyses. We used the brain donors as a blocking factor in our analyses, as they were also unique for each capture area. Data collection and analysis were not performed blind to the conditions of the experiments. Plots in R were created either in base R or with the ggplot2 R package.¹²⁸

ADDITIONAL RESOURCES

To visualize the spot-level Visium data and as a resource to the neuroscience community, we created a shiny¹²⁹ interactive browser available at https://libd.shinyapps.io/Lifespan_DG/ which is powered by the spatialLIBD v.1.15.4 R Bioconductor package.¹⁰⁶